

DEVELOPMENT OF THERMAL-VACUUM TESTING TECHNIQUES FOR SPACECRAFT AT HIGH SOLAR INTENSITIES

Interim Technical Summary Report
December 1966
CONTRACT NAS-2-3164

Prepared for
NATIONAL AERONAUTICS AND SPACE ADMINISTRATION
AMES RESEARCH CENTER
MOFFETT FIELD, CALIFORNIA

GPO PRICE \$ _____

CFSTI PRICE(S) \$ _____

Hard copy (HC) 3.00

Microfiche (MF) 1.30

ff 653 July 65

0.65

FACILITY FORM 602

N67 17185

(ACCESSION NUMBER)

91

(PAGES)

CR-73066

(NASA CR OR TMX OR AD NUMBER)

(THRU)

(CODE)

31

(CATEGORY)

Aerospace Sciences Laboratory
Lockheed Palo Alto Research Laboratory
LOCKHEED MISSILES & SPACE COMPANY
Sunnyvale, California

**DEVELOPMENT OF THERMAL-VACUUM
TESTING TECHNIQUES FOR SPACECRAFT
AT HIGH SOLAR INTENSITIES**

**Interim Technical Summary Report
December 1966
CONTRACT NAS-2-3164**

**Prepared for
NATIONAL AERONAUTICS AND SPACE ADMINISTRATION
AMES RESEARCH CENTER
MOFFETT FIELD, CALIFORNIA**

**Aerospace Sciences Laboratory
Lockheed Palo Alto Research Laboratory
LOCKHEED MISSILES & SPACE COMPANY
Sunnyvale, California**

FOREWORD

This report covers work accomplished by the Lockheed Missiles & Space Company on the Development of Thermal-Vacuum Testing Techniques for Spacecraft at High Solar Intensities (Contract NAS 2-3164) for the National Aeronautics and Space Administration, Ames Research Center, California, under the cognizance of the NASA Project Monitor, J. Kirkpatrick. The study program was carried out by the Orbit Thermodynamics Department under the administration of H. Cohan, and by the Thermophysics Laboratory under the administration of R. P. Caren.

The material presented in this report covers the results of analytical studies performed during the first 6 months of a 1-year study. Contributors to the study were:

R. E. Rolling	Thermophysics Laboratory Study Leader
G. R. Cunningham	Thermophysics Laboratory Thermal Technique Determinations
T. F. Vajta	Thermophysics Laboratory Thermal Technique Determinations
R. M. Vernon	Orbit Thermodynamics Thermal Analysis
P. W. Knopf	Orbit Thermodynamics Thermal and Computer Analysis
R. P. Warren	Orbit Thermodynamics Energy Source Analysis

PRECEDING PAGE BLANK NOT FILMED.

CONTENTS

Section		Page
	FOREWORD	iii
	ILLUSTRATIONS	vi
	TABLES	vii
	NOMENCLATURE	ix
1	INTRODUCTION	1-1
2	SPACECRAFT THERMAL ANALYSIS	2-1
	2.1 Spacecraft Configurations	2-1
	2.2 Spacecraft Environment and Orientation	2-3
	2.3 Preliminary Calculations	2-6
	2.4 Computer Thermal Analysis	2-13
3	THERMAL-VACUUM ENVIRONMENTAL SIMULATION TECHNIQUES	3-1
	3.1 Test Methods Considered	3-1
	3.2 Source Characteristics	3-2
4	FUTURE WORK	4-1
	4.1 Laboratory Investigations - Thermal Modeling	4-1
	4.2 Test Specifications	4-2
5	CONCLUSIONS	5-1
6	REFERENCES	6-1
Appendix		
A	DETAILED DESCRIPTION OF THERMAL ANALYZER PROGRAM	A-1
B	SPECULAR REFLECTION FROM RTG DISKS	B-1
C	INCIDENT HEAT FLUX VARIATION ON A CYLINDRICAL SURFACE EXPOSED TO REFLECTED AND NONREFLECTED LINE SOURCES	C-1

ILLUSTRATIONS

Figure		Page
2-1	Solar-Powered Configuration	2-2
2-2	RTG-Powered Configuration	2-4
2-3	Solar Heat Flux on Flat Plate, 0.20 Perihelion Solar Probe	2-5
2-4	Coordinate System for Determination of Temperature Distribution on a Rotating Hollow Cylinder	2-9
2-5	Finite Solar Disk Diameter and Satellite Attitude Misalignment	2-11
2-6	Temperature Distribution for Solar-Powered Configuration at 1.0 and 0.2 A. U.	2-16
2-7	Temperature Distribution for RTG-Powered Configuration at 1.0 and 0.2 A. U.	2-18
2-8	Platform Temperature Versus Thermal Resistance	2-19
3-1	Directional Intensity Variation of Reflected and Unreflected Tubular Quartz Envelope Tungsten Filament Lamp	3-10
3-2	Directional Radiation Properties, Reflected Lamps	3-11
3-3	Spectral Reflectance of Spacecraft Materials	3-12
3-4	Spectral Reflectance of Spacecraft Materials	3-13
3-5	Error in Equilibrium Temperature for Constant Simulator Output	3-17
A-1	Thermal Analyzer Model Node Locations	A-2
A-2	Honeycomb Schematic	A-8
A-3	Effective Louver Emittance as a Function of Instrument Platform Temperature	A-12
B-1	Specular Reflection Diagram	B-2
C-1	Lamp Array Geometry	C-2
C-2	Energy Distribution on Cylindrical Surface	C-6
C-3	Energy Distribution on Cylindrical Surface	C-7
C-4	Energy Distribution on Cylindrical Surface	C-8

TABLES

Table		Page
2-1	Spacecraft Equilibrium Temperatures	2-7
2-2	Effect of Satellite Misalignment	2-12
2-3	Thermal Analyzer Model Node List	2-14
2-4	Effect of Multilayer Insulation Thermal Conductivity on Instrument Platform Temperature	2-20
3-1	Potential Errors Attributable to Energy Source Characteristics for Surface Temperature Simulation	3-3
3-2	Potential Errors Attributable to Energy Source Characteristics for Absorbed Heat Flux Simulation	3-4
3-3	Potential Errors Attributable to Energy Source Characteristics for Solar Spectral Energy Simulation	3-5
3-4	Characteristics To Be Considered in Selection of Energy Source	3-6
3-5	Main Data of High Wattage Xenon, Mercury, and Mercury-Xenon Compact Arc Lamps	3-7
3-6	Main Data of High Wattage Xenon, Mercury, and Mercury-Xenon Compact Arc Lamps	3-8
3-7	Energy Absorption Data - Silicon Solar Cell	3-14
3-8	Energy Absorption Data - Optical Solar Reflector	3-15
3-9	Temperature Errors for Argon and Carbon Arc Sources	3-16
A-1	Solar Heat Rates to External Surfaces at 1 A. U. , Solar-Powered Configuration	A-5
A-2	Solar Heat Rates to External Surfaces at 1 A. U. , RTG-Powered Configuration	A-6
A-3	Heat Sources Internal to Vehicle	A-7
A-4	Thermal Conduction Resistances	A-9
A-5	Thermal Radiation Exchange Factors	A-13
C-1	Energy Distribution on a Cylindrical Surface for a Cosine Variation in Intensity About the Axis of Line Source	C-3

Table		Page
C-2	Energy Distribution on a Cylindrical Surface as Received From Line Source Radiating Uniformly in all Directions	C-4
C-3	Energy Distribution on a Cylindrical Surface for an Intensity Variation of $e^{-(6\phi/\pi)} \cos \phi$ About the Axis of a Line Source	C-5
C-4	Lamp Angle and Heat Flux for Specific Locations on Specimen – Cosine Intensity Variation About Source Axis	C-9
C-5	Lamp Angle and Heat Flux for Specific Locations on Specimen – Intensity Uniform About Lamp Axis	C-10
C-6	Lamp Angle and Heat Flux for Specific Locations on Specimen – $e^{-(6\phi/\pi)} \cos \phi$ Intensity Variation About Source Axis	C-11

NOMENCLATURE

A. U.	astronomical unit, average earth's distance from sun
A_p	area projected toward the sun
A_{TOT}	total surface area
A_i	area of node i
a	distance from sun to spacecraft
D	thermal diffusivity, $k/\rho c_p$ (ft^2/hr)
G_s	solar heat flux density
h	height of cylinder backside irradiated by sun
k	thermal conductivity ($\text{Btu/hr-ft-}^\circ\text{F}$)
Q	heat flux
R_s	radius of sun
R_{ij}	thermal resistance between nodes i and j ($\text{sec-}^\circ\text{F/Btu}$)
r	radius of cylinder
s	cylinder wall thickness
F_{ij}	view factor between nodes i and j
T	temperature
T^*	maximum temperature
\bar{T}	average temperature
T_s	temperature of space
T_v	vehicle temperature in space

T_{vs}	vehicle temperature in simulated space environment
T_w	temperature of vacuum chamber cold wall
v_o	dimensionless velocity
α_s	absorptance to simulated solar radiation
α_o	solar absorptance
ϵ	infrared emittance
η^*	angular location of maximum cylinder temperature
ρ_o	dimensionless radius
σ	Stefan-Boltzmann constant
β	angular location of RTG boom
ϕ	phase angle defined in Eq. (2.4), attitude misalignment angle, polar angle about lamp axis
θ	angle between satellite-sun line and line from edge of solar disk, defined in Fig. 2-5
ψ	angle defined by $\theta + \phi$
ρ	density of material (lb/ft ³)
c_p	specific heat (Btu/lb-°F)

Section 1

INTRODUCTION

Thermal testing of space vehicles prior to launch is a necessary procedure to evaluate thermal design and to ascertain that all electrical and mechanical systems will remain within specified temperature limits throughout the prescribed mission. In many cases thermal testing may be performed on the complete vehicle system in a simulation chamber which has collimated solar simulation, high vacuum, and a cold wall "space sink." Under such ideal circumstances, it is possible to observe directly the vehicle thermal and operational behavior and make design changes as required. However, vehicle configurations can arise where long booms, large paddles, antenna, or other protuberances may require thermal testing of individual components and then simulation of their effects during thermal testing of the main payload area. In this event the test procedure is not straightforward and requires individual solution to each particular problem. However, component simulation testing, when carefully applied, has proved to be reliable and sufficiently accurate for prediction of space thermal behavior.

The anticipated use of satellites which approach to within 0.18 A. U. of the sun introduces a whole new set of problems related to the required thermal test procedures. Simulation chambers with capabilities for providing solar simulation at the high solar intensities to be encountered during solar probe missions are presently nonexistent. Considerable progress has been made in producing test facilities with solar simulation capability of up to 2 suns; however, development of these facilities has been accomplished at tremendous expense, which provides an indication of the probable costs involved in producing simulation of the 30-sun intensity for an 0.18 A. U. mission.

This interim report presents the results of analytical studies and preliminary investigations directed toward the specification of test procedures and techniques to be used for high-intensity thermal testing of a solar probe spacecraft. The initial

effort consisted of analyzing the spacecraft thermal response in the anticipated environment for the solar probe mission. Results of this analysis yielded analytical thermal models of two candidate configurations which may be used for predicting spacecraft temperature response under actual and simulated thermal-vacuum environmental conditions. Complete details of the thermal models and their application for solution by computer are provided herein. A second major area of study was the investigation of methods for simulating the environmental conditions during thermal-vacuum testing of the spacecraft. Energy source characteristics for the methods of simulation were determined for a limited number of sources, and a preliminary estimate of temperature error due to spectral mismatch between solar simulation sources and the sun's spectral energy distribution has been made. Work is continuing to provide a more detailed estimate of the adequacy of the various simulation methods. Also, work is continuing on the measurement of additional lamp spectral output data and on investigation of the applicability of thermal modeling to environmental testing of spacecraft at high thermal intensities. Additional activity planned for the remaining portions of the program is described in Section 4.

Section 2

SPACECRAFT THERMAL ANALYSIS

The primary objectives of this analysis were to determine the temperature distributions within the two proposed spacecraft configurations for the anticipated space environmental conditions and to determine the sensitivity of these temperatures to variations in incident heat flux and joint resistances. The analytical procedure, a summary of the major results obtained, and the methods used for checking the results are described in the following subsections. A detailed description of the thermal analyzer model used in the thermal analysis, including assumptions made in determining the thermal conductance and radiation resistances, is presented in Appendix A.

2.1 SPACECRAFT CONFIGURATIONS

2.1.1 Solar-Powered Configuration

The solar-powered configuration is modeled after the Pioneer³ spacecraft. Major differences are the addition of a despun antenna reflector, addition of a variable-opening lower solar array shield, and application of an Optical Solar Reflector (OSR) thermal control coating to all solar exposed surfaces except the solar panels and the reflecting side of the antenna reflector. Major subdivisions of the vehicle are:

- (1) Antenna and reflector
- (2) Three booms
- (3) Solar cell arrays and lower solar cell shield
- (4) Control and experiment section
- (5) Louver system and lower enclosure

A sketch of the solar-powered configuration is shown in Fig. 2-1.

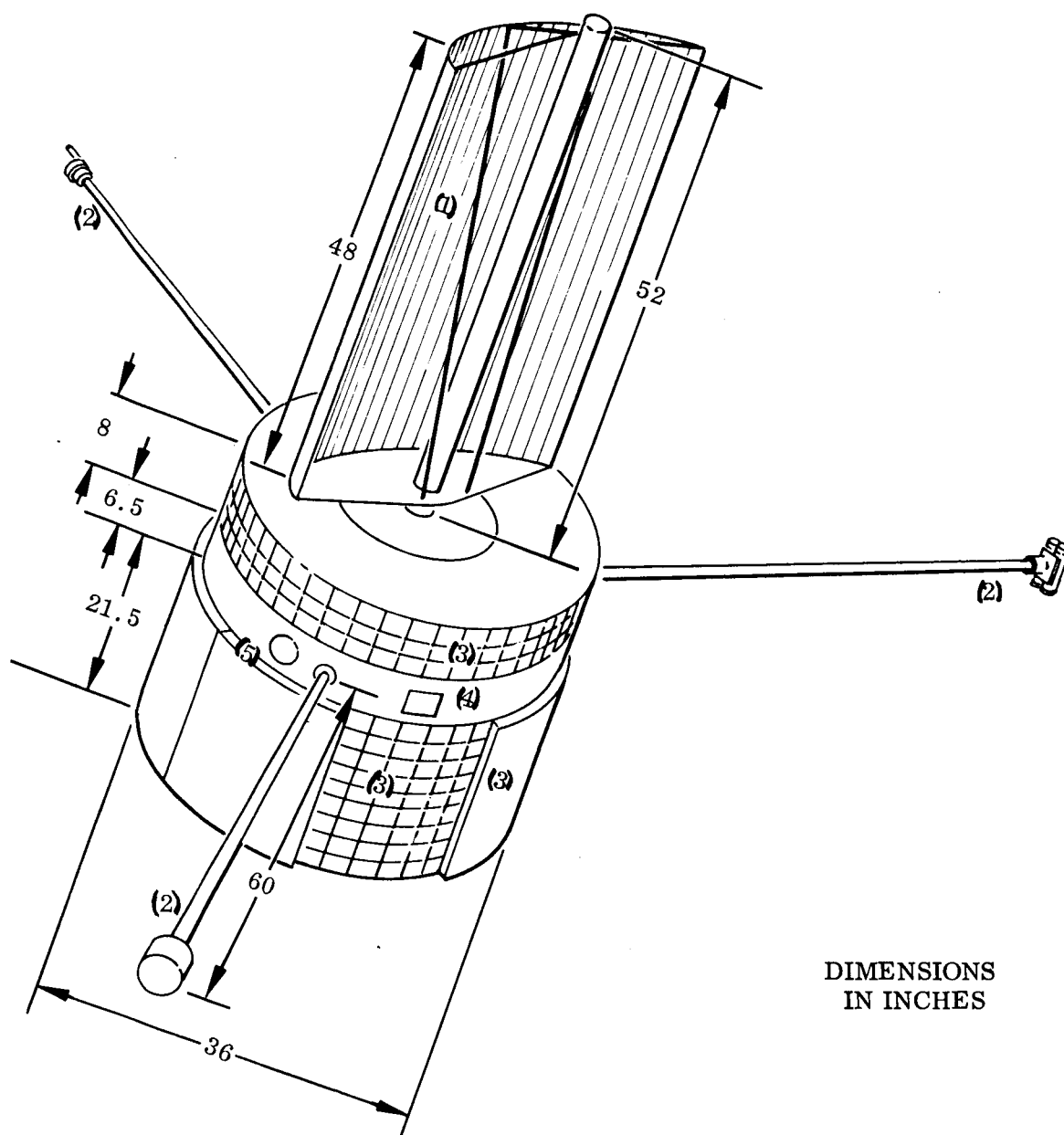


Fig. 2-1 Solar-Powered Configuration

2.1.2 Radioisotope Thermoelectric Generator (RTG)-Powered Configuration

The RTG-powered configuration is also modeled after the Pioneer~~V~~ spacecraft. Major differences are the addition of a despun antenna reflector, removal of the solar cells and associated equipment, shortening of the lower enclosure by 7-3/4 in., addition of two boom-mounted 30-W RTG's, and application of an OSR coating to all solar-exposed surfaces other than the reflecting side of the antenna reflector. Major subdivisions of the RTG-powered vehicle are:

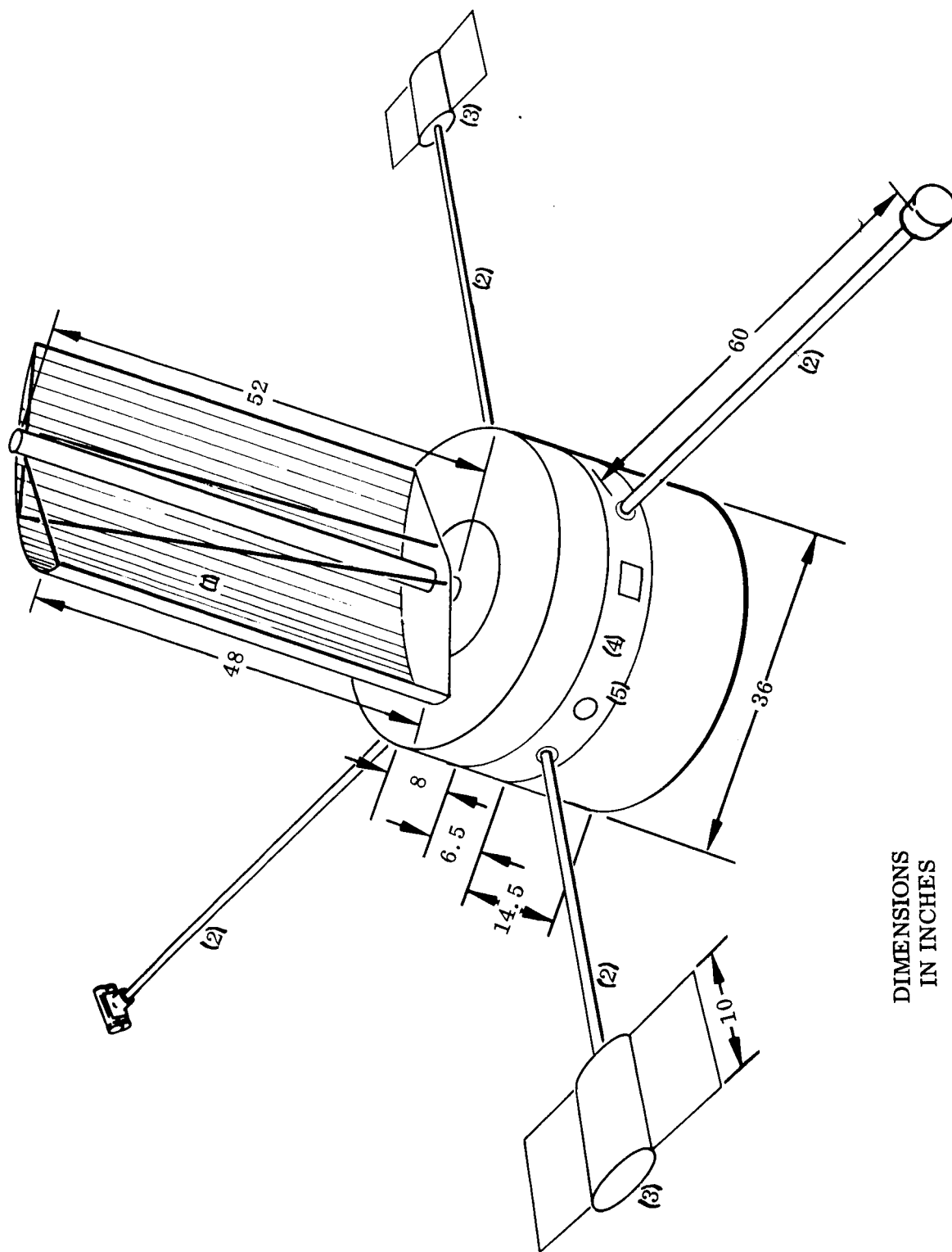
- (1) Antenna and reflector
- (2) Four booms
- (3) Two RTG's
- (4) Control and experiment section
- (5) Louver system and shortened lower enclosure

A sketch of the RTG-powered configuration is shown in Fig. 2-2.

2.2 SPACECRAFT ENVIRONMENT AND ORIENTATION

For purposes of the thermal analysis, both the solar-powered and RTG-powered spacecraft were assumed to be moving in elliptical orbit about the sun, with perihelion at 0.2 A. U. and aphelion at 1.0 A. U. The orbits were assumed to be in the plane of the ecliptic, and both spacecraft were assumed to be spin stabilized at 60 rpm with the axis of spin normal to the plane of the ecliptic. The despun antenna reflectors face the earth.

The ultraviolet, visible, and infrared radiation fluxes at 1.0 A. U. were taken to be those due solely to solar radiation. The data of Johnson (Ref. 1) were used to specify the spectral distribution of solar radiation in these regions. The spectral distribution of solar radiation was taken to be the same at 0.2 A. U. as at 1.0 A. U.; however, the magnitude of the solar radiation flux increases as the inverse square of the distance from the sun (assuming the sun to be a point source). Thus, as shown in Fig. 2-3, the



DIMENSIONS
IN INCHES

Fig. 2-2 RTG-Powered Configuration

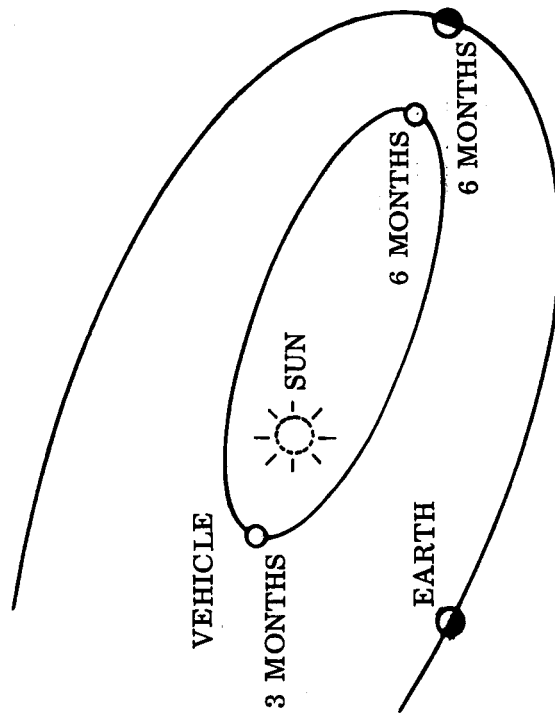
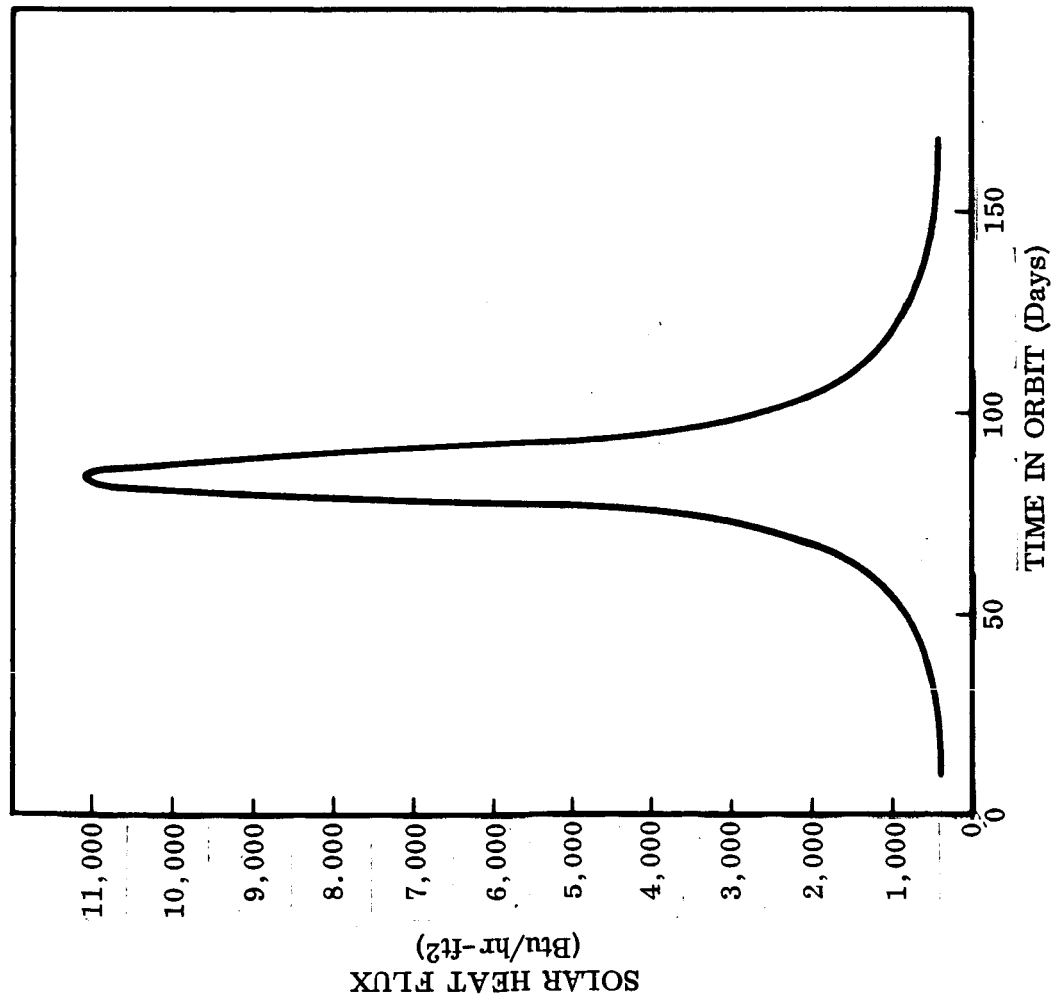


Fig. 2-3 Solar Heat Flux on Flat Plate, 0.20 Perihelion Solar Probe

solar flux incident on a flat plate increases by a factor of 25 as the distance from the sun is reduced from 1.0 to 0.2 A. U.

The thermal analysis which is described did not account for several real effects which would be encountered as the spacecraft approaches the sun. Since the sun is not in reality a point source but a spherical mass of varying optical density, the radiation flux incident on a spacecraft at 0.2 A. U. appears to come from a disk whose angular diameter is 2.67 deg (0.53 deg at 1.0 A. U.). The effect of this finite solar disk diameter was not considered in the computer analysis, but an estimate of the magnitude of the resultant error in computed temperatures was performed and is discussed in subsection 2.3.3; also discussed is the effect on spacecraft temperatures of misalignment in vehicle attitude. Additional assumptions made in the analysis were that spacecraft thermal properties are independent of temperature and that optical and thermal radiation properties are not degraded by exposure to high temperatures, vacuum, or solar radiation.

2.3 PRELIMINARY CALCULATIONS

To provide an independent check on the computer results, brief hand calculations were performed for selected portions of the prototype spacecraft. Also, estimates of the importance of solar radiation reflected from boom-mounted experiments onto the cylindrical body of the spacecraft were made. The following subsections discuss the results of these analyses and their influence on the thermal analyzer computer inputs.

2.3.1 Selected Equilibrium Temperatures

Hand calculations of equilibrium temperatures for the cylindrical spacecraft shell were performed for various solar distances between 0.18 and 1.0 A. U. For an infinitely long circular cylinder whose axis is normal to the direction of incident solar flux, the equilibrium surface temperature is computed from the following heat balance:

$$G_s \alpha_o A_P - \sigma A_{TOT} \epsilon \bar{T}^4 = 0 \quad (2.1)$$

where

$$\frac{A_P}{A_{TOT}} = \frac{\text{area projected to sun}}{\text{total surface area}} = \frac{1}{\pi}$$

Solving the equation for \bar{T} ,

$$\bar{T} = 100(1.857 G_s \alpha_o / \epsilon)^{1/4} \quad (2.2)$$

The solar heat flux G_s is given as a function of distance from the sun in Fig. 2-3. Temperatures computed from Eq. (2.2) are shown in Table 2-1 for cylindrical surfaces covered with OSR ($\alpha_o / \epsilon = 0.10/0.80$) or solar cells ($\alpha_o / \epsilon = 0.72/0.80$).

Table 2-1
SPACECRAFT EQUILIBRIUM TEMPERATURES^(a)

Solar Distance (A. U.)	G_s (W/cm ²)	$\bar{T}_{\text{Solar Cell}}$ ^(b) (° F)	\bar{T}_{OSR} ^(c) (° F)
0.18	4.32	760	300
0.20	3.50	690	257
0.50	0.56	277	-10
0.80	0.22	140	-107
1.00	0.14	60	-141

(a) Average temperature of an infinitely long circular cylinder whose axis is normal to the ecliptic plane.

(b) $\alpha_o = 0.72$, $\epsilon = 0.82$.

(c) $\alpha_o = 0.10$, $\epsilon = 0.80$.

2.3.2 Validity of Quasi-Steady-State Analysis

The temperatures shown in Table 2-1 are equilibrium temperatures which would exist if the spacecraft were spinning at an infinite circumferential velocity with its spin axis normal to the plane of the ecliptic. (End losses from the cylindrical section are neglected, since preliminary calculations were performed for an infinitely long cylinder.) The thermal analyzer computations were based on the same assumption, namely, that the circumferential variations in temperature around the spacecraft due to its finite spin rate are negligibly small. To estimate the error incurred by this assumption, the actual temperature variation around an assumed cylinder having a very low thermal capacitance was computed. This cylinder was assumed to be a single layer of aluminized Mylar coated with OSR; the axis of the cylinder was assumed to be normal to the solar flux; and a cylinder spin rate of 60 rpm was assumed. Referring to the coordinate system shown in Fig. 2-4, location of the maximum temperature is obtained by solving the following equation for η^* (Ref. 2):

$$\frac{\rho_o}{v_o} (\eta^* - 1) = 2 [\pi \cos (2\pi\eta^* - \phi) - 1] \quad (2.3)$$

where

$$\begin{aligned} \rho_o &= \text{dimensionless radius} = r/R \\ R &= \text{thermal radius} = (sk\bar{T}/16\pi\alpha_o G_s)^{1/2} \\ \bar{T} &= \text{average temperature} = (\alpha_o G_s / \pi \epsilon \sigma)^{1/4} \\ v_o &= \text{dimensionless velocity} = v/v^* \\ v &= \text{circumferential velocity} \\ v^* &= \text{thermal velocity} = D/\pi R \end{aligned}$$

and

$$\phi = \tan^{-1} \left[\frac{1}{2} \frac{(\rho_o/2\pi)^2 + 1}{v_o(\rho_o/2\pi)} \right] \quad (2.4)$$

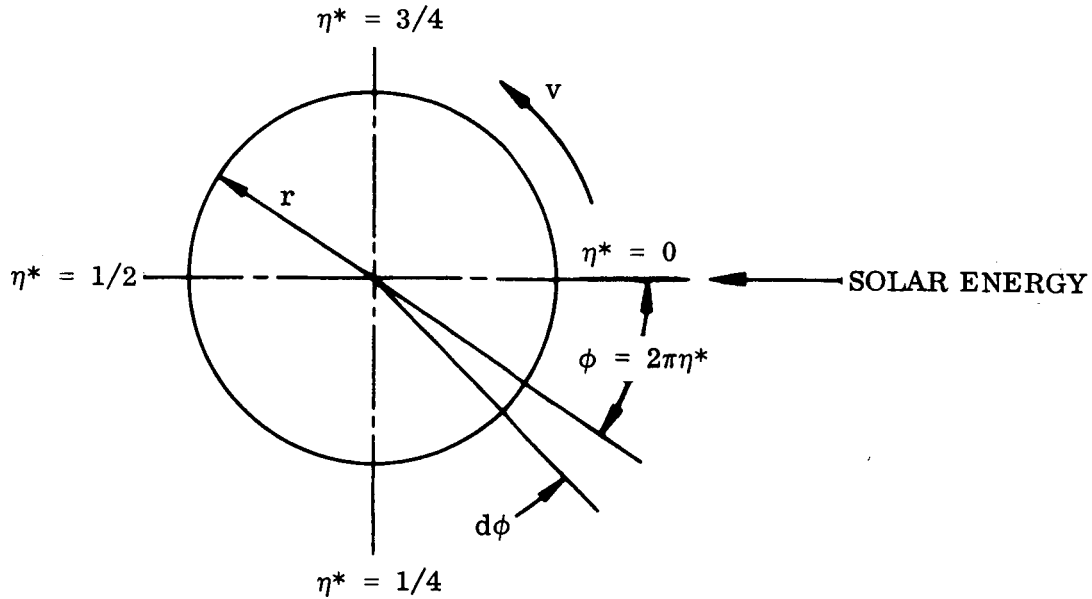


Fig. 2-4 Coordinate System for Determination of Temperature Distribution on a Rotating Hollow Cylinder

The resultant maximum temperature is given by

$$\frac{T^*}{\bar{T}} = 1 + \frac{\rho_0}{16v_0} \left[2(\eta^* - 1) + \frac{\rho_0}{2v_0} (\eta^* - 1)^2 - \sin(2\pi\eta^* - \phi) \right] \quad (2.5)$$

The aluminized Mylar cylinder was assumed to have a diameter of 4 ft and a thickness of 0.001 in. For these dimensions the location of the maximum temperature point is at $\eta^* = 0.805$ (i. e., 290 deg), and the resultant mean temperature at 0.2 A. U. is 770° F. The temperature variation about this mean, computed from Eq. (2.5), is $\pm 11^\circ$ F. This temperature variation is equivalent to an incident heat flux variation of $\pm 730 \text{ Btu/hr-ft}^2$, or ± 6.6 percent of the average insolation at 0.2 A. U. and is considered to be the largest error that might be attributed to the quasi-steady-state analyses.

2.3.3 Effect of Finite Solar Disk Diameter and Misalignment in Satellite Attitude

The additional satellite projected area illuminated by the sun due to the solar field angle and misalignment of the satellite from the plane of the ecliptic can give rise to an appreciable energy flux absorbed by the satellite.

Figure 2-5 describes the geometry concerned and shows the maximum height h along the inner wall of the satellite at which this effect is experienced. Calculation of the satellite projected area illuminated due to solar rays emitting from the bottom rim of the photosphere makes use of the following fixed parameters:

$$R_s = 2.2826 \times 10^9 \text{ ft}$$

$$r = 3.0 \text{ ft}$$

$$a = 0.18 \text{ A. U.} = 8.83 \times 10^{10} \text{ ft}$$

$$\theta \doteq \tan^{-1} \theta = R_s/a = 0.0259 \text{ rad} = 1.485 \text{ deg}$$

The projected area, assuming the sun's rays to be parallel to a line from the bottom of the photosphere to the center of a circular opening in the bottom of the satellite, is given by

$$A_p = \frac{\pi r^2}{2} \tan \psi$$

The maximum height of solar energy impingement on the inner surface of the cylinder is

$$h = 2r \tan \psi$$

where

$$\psi = \theta + \phi$$

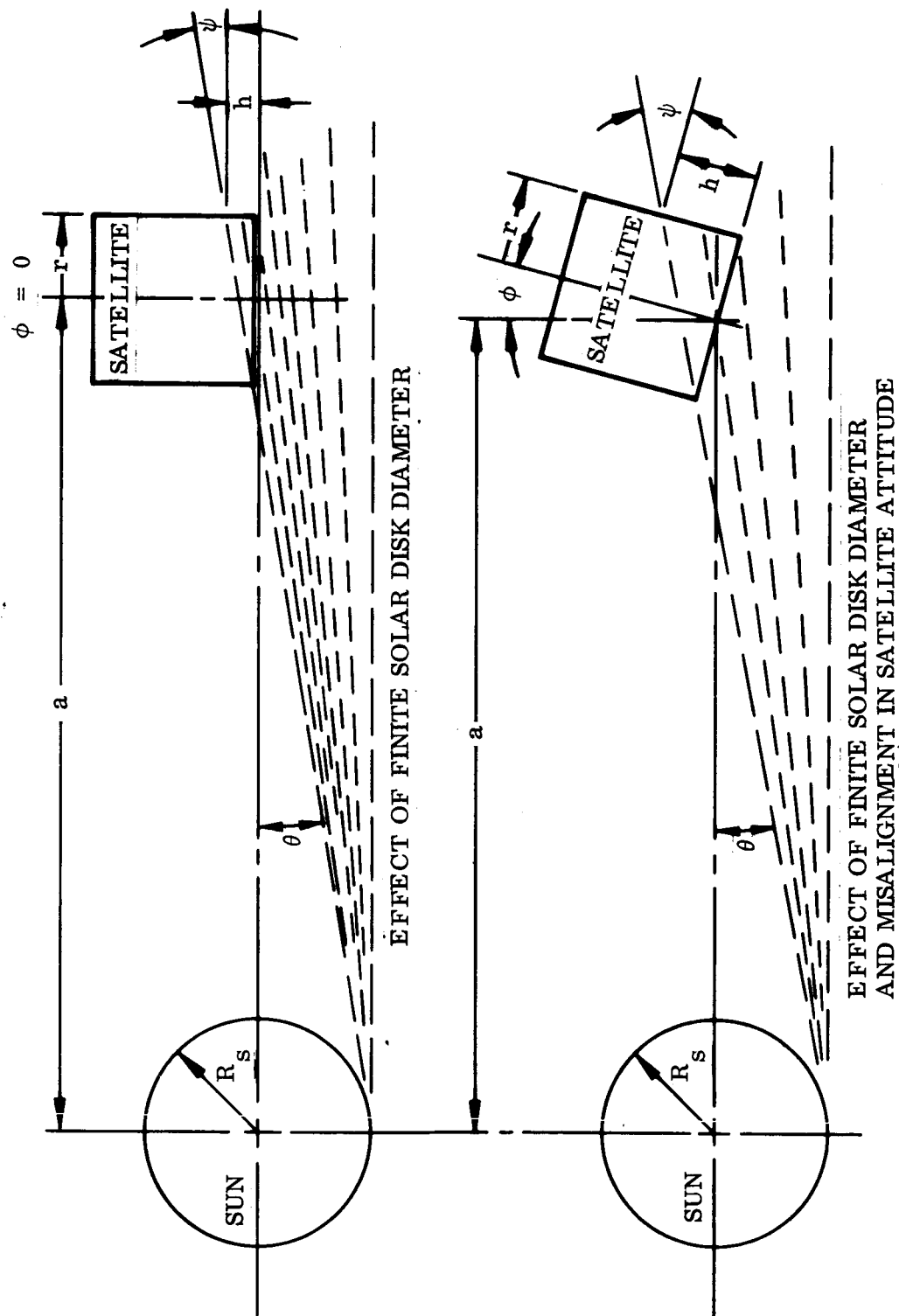


Fig. 2-5 Finite Solar Disk Diameter and Satellite Attitude Misalignment

For no misalignment, $\phi = 0$, the power impinging on the inner surface at 0.2 A. U. is about 300 W and $h = 0.925$ in. For increasing misalignment, the effect is as shown in Table 2-2.

Table 2-2
EFFECT OF SATELLITE MISALIGNMENT

ϕ (deg)	ψ (deg)	$\tan \psi$ (rad)	A_p (ft ²)	h		Power (W) at 0.2 A. U. Assuming $\theta = 1.5$ deg
				(ft)	(in.)	
0	1.5	0.0259	0.092	0.077	0.925	300
0.5	2.0	0.0349	0.124	0.105	1.3	400
1.0	2.5	0.0437	0.154	0.131	1.57	500
2.0	3.5	0.0612	0.217	0.183	2.2	705
5.0	6.5	0.1140	0.403	0.342	4.1	1310

The additional power inputs shown in Table 2-2 were calculated assuming the energy impinging on the inner surface to be 25×443 Btu/hr-ft² at 0.2 A. U. This assumption neglects losses due to shadowing of the solar disk; therefore, the calculated values for power input are higher than would actually be the case. This brief analysis serves to illustrate that a problem may exist, but a more rigorous analysis should be performed before design changes are made to compensate for the effect. If changes prove to be necessary, one method of reducing the additional power input would be to add a specular reflecting surface fixed to the lower array frame. This surface should be canted by an angle equal to $(\phi_{\max} + 1.5 \text{ deg})$ from the cylinder axis and should be at least as high as h_{\max} to reflect the incident solar energy back out of the bottom of the satellite.

2.3.4 Effect of Specular Solar Reflections and Shadowing

Solar radiation reflected specularly from the RTG disks facing the satellite is less than 0.4 percent of the average direct solar radiation impinging on the bellyband section of the satellite. This result, from the analysis described in Appendix B, corrects

a previously reported result that no energy was reflected to the satellite. Other specular surfaces of the RTG-powered or solar-powered configurations are either not aligned to reflect solar radiation back to the satellite or are small compared with the RTG disks analyzed.

This result is significant from the standpoint of establishing test specifications and source requirements, since it implies that the simulation of a band of high-intensity radiation concentrated at the equator of the satellite will not be necessary during environmental testing.

2.4 COMPUTER THERMAL ANALYSIS

2.4.1 Computer Model Description

Two analytical models of the solar-powered and the RTG-powered configurations were constructed for predicting the temperature response to vehicle-sun distances of 1.0 and 0.2 A.U. These models were constructed from 43 nodes and 45 nodes, respectively, and were connected by conduction and radiation resistors calculated or approximated from the available Pioneer spacecraft description, supplemented by design changes proposed by NASA-Ames personnel. The node allocation listing is given in Table 2-3. A detailed description of the electrical analog network is presented in Appendix A. The important assumptions involved in the node allocation and resistance determinations are listed below.

General Assumptions

- There is no temperature variation around the circumference of the vehicle. This assumption is based on the vehicle symmetry and results of quasi-steady-state preliminary calculations described in subsection 2.3.2.
- The equipment platform is assumed to be symmetrical, and the majority of equipment is combined into one node. Experiments that are directly exposed to the external environment are separated according to their window surface characteristics.

Table 2-3

THERMAL ANALYZER MODEL NODE LIST

<u>Node</u>	<u>Description</u>	<u>Node</u>	<u>Description</u>
1	Space	28	Sun Sensor, Outside
2	Gas Bottle	29	Chicago and GRCSW Experiment, Outside
3	DTU Equipment Package	30	Ames Experiment, Outside
4	Average Equipment Package	31	MIT Experiment, Outside
5	MIT Experiment	32	Bellyband Insulation, Inner Surface
6	Ames Experiment	33	Bellyband Insulation, Middle
7	Chicago and GRCSW Experiment	34	Bellyband Insulation, Outer Surface
8	Sun Sensors	35	Control and Experiment Boom, Base
9	Control and Experiment Boom Bracket	36	Control and Experiment Boom, Middle
10	Upper Platform	37	Control and Experiment Boom, End
11	Lower Platform and Louvers	38	Lower Array, Forward, Insulation Surface
12	Cylinder Insulation Surface	39	Lower Array, Forward, Insulation Middle
13	Cylinder Inner Surface	40	Lower Array, Forward, Outside
14	Gas Bottle Insulation Surface	<u>SOLAR POWERED ONLY</u>	
15	Antenna Base Supports, Solar	41	Lower Array, Aft, Insulation Surface
16	Antenna Base and Motor	42	Lower Array, Aft, Insulation Middle
17	Antenna Platform	43	Lower Array, Aft, Outside
18	Antenna Dipole, Lower	<u>RTG POWERED ONLY</u>	
19	Antenna Dipole, Upper	41	RTG Boom Bracket
20	Antenna Reflector, Lower	42	RTG Boom, Base
21	Antenna Reflector, Upper	43	RTG Boom, Middle
22	Top Cover, Inside	44	RTG Boom, End including RTG
23	Top Cover, Outside	45	Antenna Base Supports, RTG
24	Upper Frame		
25	Upper Array, Insulation Surface		
26	Upper Array, Insulation Middle		
27	Upper Array, Outside		

- The louver system operates uniformly under all sections of the equipment platform, and there is no temperature gradient through the louvers.
- The louver system operation is approximated by varying the emittance of the underside of the equipment platform linearly with the platform underside surface temperature.
- Solar heat rates into all exposed surfaces are approximated by the average over one complete vehicle revolution.
- Internal power dissipation is assumed constant at 50 W.

Assumptions Pertaining to Solar-Powered Configuration Only

- The lower solar array is surrounded by a despun variable aperture radiation shield that is conductively insulated from the vehicle and whose inner surface is in thermal equilibrium with the solar array. At a distance of 0.2 A. U. from the sun, the aperture is such as to hold the solar array at 190° F.
- The three booms are combined into one boom by multiplying the combined thermal resistance by 1/3.

Assumptions Pertaining to RTG-Powered Configuration Only

- The solar arrays are replaced with the OSR thermal control surface.
- The lower array section is shortened 7-3/4 in.
- The four booms (two RTG booms and two instrument booms) are simulated by two equivalent booms, each having twice the actual input energy flux and half the actual boom thermal resistance.

2.4.2 Results of Basic Analysis

Solar-Powered Configuration. Temperatures of the equipment and equipment platform were close enough to be considered as a single temperature level in discussing the response of the configuration to varying boundary conditions and design changes. At 1.0 A. U., this level is 52° F and at 0.2 A. U. it is 68° F. Figure 2-6 shows

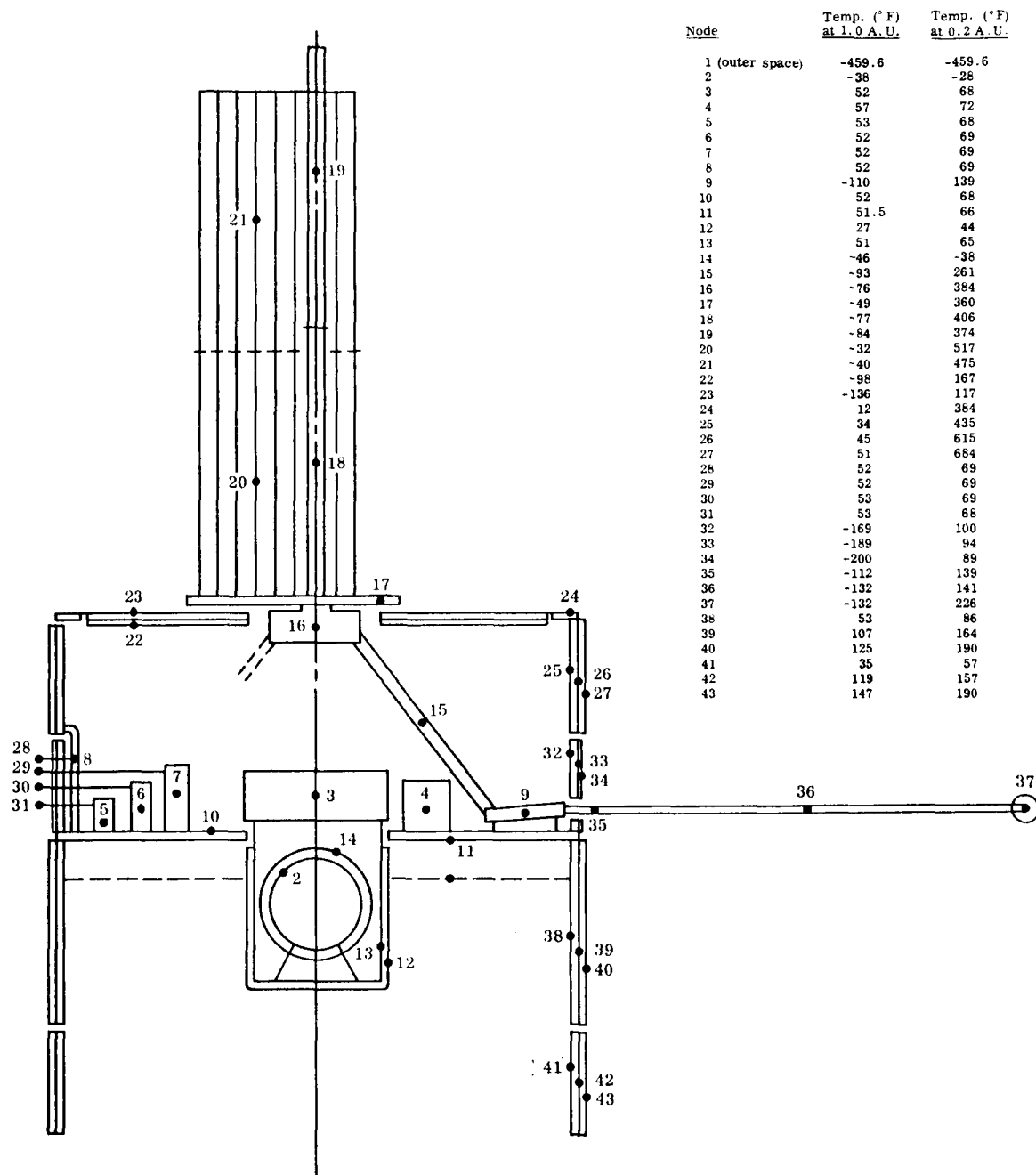


Fig. 2-6 Temperature Distribution for Solar-Powered Configuration at 1.0 and 0.2 A.U.

individual node temperatures. These temperatures compare well with available Pioneer VI flight data. Heat fluxes are on the order of 1 W or less except as follows:

	<u>1.0 A. U.</u>	<u>0.2 A. U.</u>
Out through the louvers	42 W	81 W
In through experiment windows	—	14
In through the upper solar array by way of sun sensor bracket	—	12
To platform from equipment	50	50

RTG-Powered Configuration. In this configuration, a single temperature level for the instrument platform can also be assumed in discussing vehicle thermal response. At 1.0 A. U. the level is 51° F, and at 0.2 A. U. it is 67° F. Figure 2-7 shows individual node temperatures.

Heat fluxes are on the order of 1 W or less except as follows:

	<u>1.0 A. U.</u>	<u>0.2 A. U.</u>
Out through the louvers	39 W	66 W
In through experiment windows	—	14
To platform from equipment	50	50

2.4.3 Effects of Parameter Variations

Conductive resistances surrounding the boom brackets were varied over a wide range of values for the 0.2 A. U. environment. Results of these variations show that changes in spacecraft instrument platform temperature are negligible. This is primarily caused by the predominating effect of equipment power dissipation and louver temperature control in maintaining stable platform temperatures.

Conductive thermal resistances between the upper solar array substrate and sun-sensor brackets were also varied over a wide range. The effect of these variations on platform temperature is shown in Fig. 2-8 for the solar-powered configuration. It may be seen

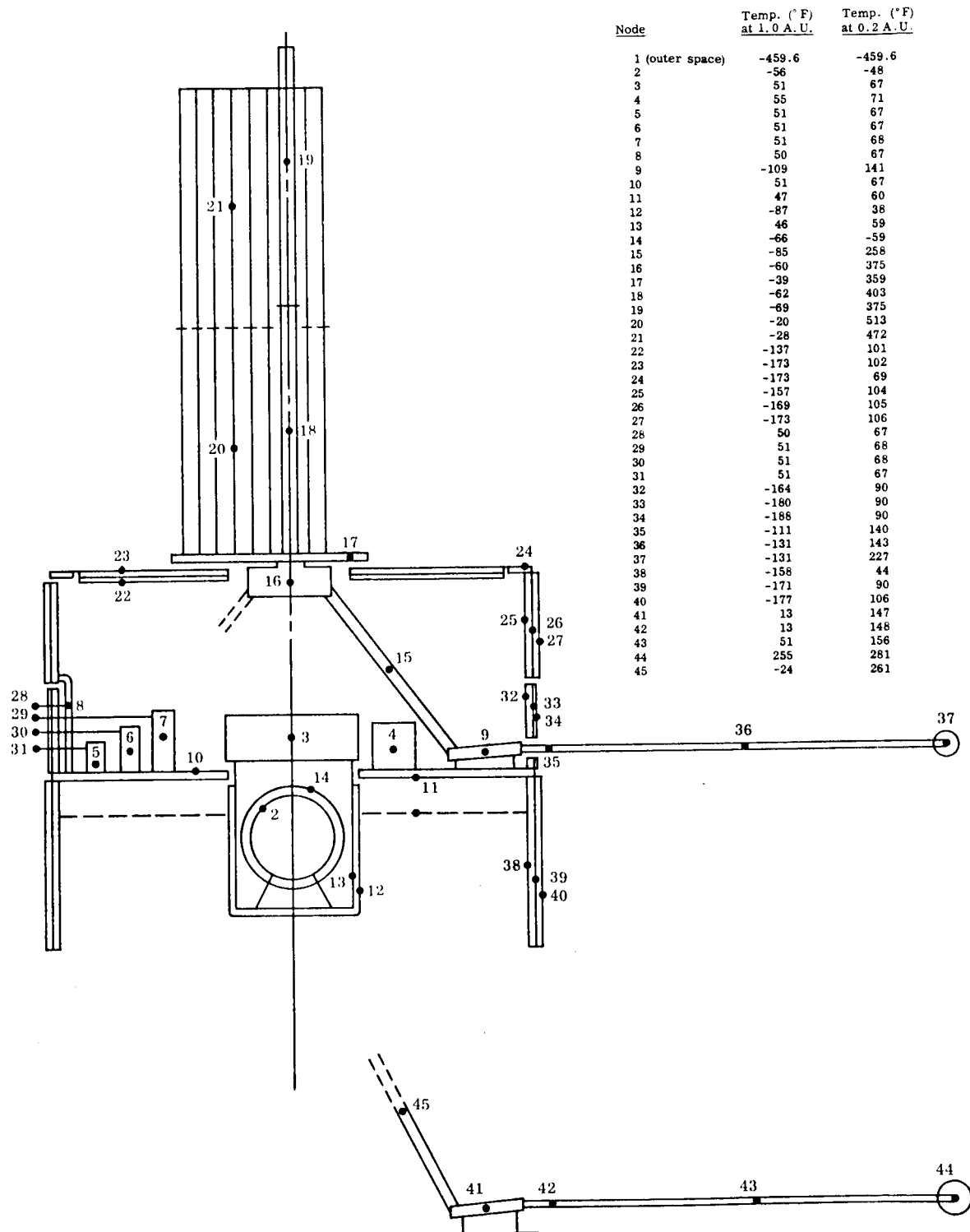


Fig. 2-7 Temperature Distribution for RTG-Powered Configuration at 1.0 and 0.2 A.U.

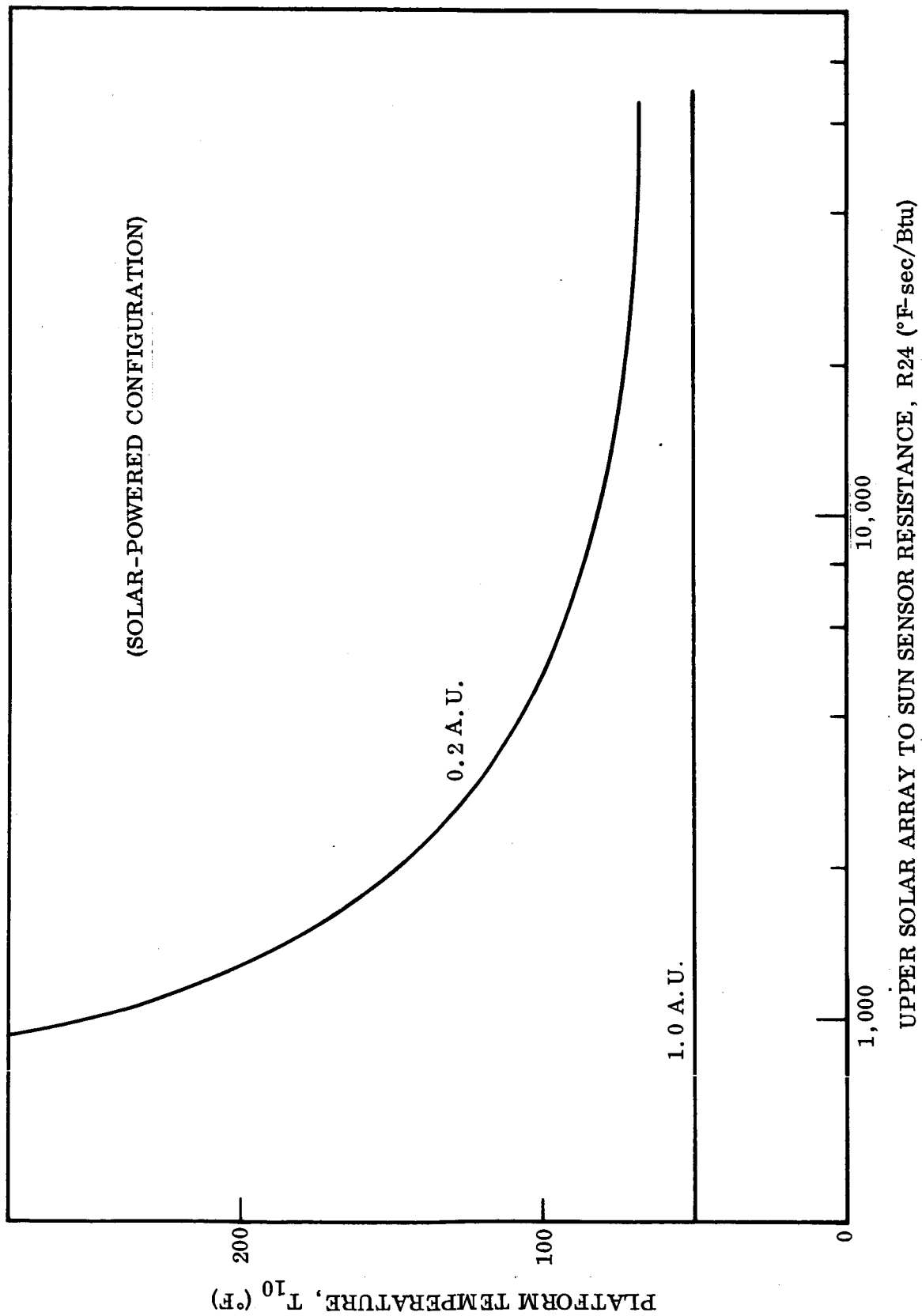


Fig. 2-8 Platform Temperature Versus Thermal Resistance

that, at 1.0 A. U., variations in conduction resistance have no effect on platform temperature. This result is reasonable in view of the low-energy flux through the sun-sensor bracket at 1.0 A. U. as indicated. At a solar distance of 0.2 A. U., however, the platform temperature increases rapidly with decreasing thermal resistance owing to the large heat flux absorbed by the unshielded upper solar array. To obtain acceptable platform temperatures, it was necessary to specify a large thermal resistance between the upper solar array substrate and the sun-sensor brackets.

Variations in instrument platform temperature due to changes in multilayer insulation effective thermal conductivity were determined. Thermal conductivities of 5×10^{-3} Btu/hr-ft-° F and 5×10^{-5} Btu/hr-ft-° F were considered, and results were compared with the platform temperature obtained using 5×10^{-4} Btu/hr-ft-° F. Variations in platform temperature are small, as shown in Table 2-4.

Table 2-4
EFFECT OF MULTILAYER INSULATION THERMAL CONDUCTIVITY
ON INSTRUMENT PLATFORM TEMPERATURE

Effective Conductivity (Btu/hr-ft-° F)	Orbit	
	1.0 A. U.	0.2 A. U.
5×10^{-3}	52.7° F	81.0° F
5×10^{-4}	52.4	80.0
5×10^{-5}	52.3	78.5

Section 3

THERMAL-VACUUM ENVIRONMENTAL SIMULATION TECHNIQUES

This section discusses the results of preliminary investigations into techniques that may be employed during thermal-vacuum testing of the solar probe spacecraft. The results obtained thus far do not allow specification of detailed testing procedures, but they do provide an indication of the important items that must be considered in selecting optimum simulation techniques.

3.1 TEST METHODS CONSIDERED

Three general approaches to the thermal simulation problem were considered during the study:

- Surface temperature simulation
- Absorbed heat flux simulation
- Solar spectral energy input simulation

In the first method, analytically calculated orbital spacecraft temperatures are reproduced in a vacuum chamber by the use of any one or a combination of energy sources; these may include infrared lamps, resistance heaters on the spacecraft outer skin, heater blankets, etc., the heat input being controlled by temperature monitors on the spacecraft skin. Similarly, in the second method, a variety of energy sources may be used to reproduce analytically calculated flux rates absorbed by the spacecraft outer surfaces. This method requires knowledge of the optical properties of the spacecraft outer surface as well as the spectral distribution of the energy source. Thus, both methods 1 and 2 rely on experimental measurements in conjunction with analytical calculations. In the third method, usually described as "solar simulation" testing, an energy source is used whose spectral intensity approximates that which the spacecraft would experience from solar radiation. Obviously, the first method relies almost wholly on an accurate thermal analysis of the spacecraft, whereas the third method

imposes the most stringent requirement on the degree of simulation obtained from the energy source. Methods 1 and 2 have been used extensively. Reference 3 describes the first approach and includes a comparison of flight behavior and the test results. A sophisticated approach to the second method is described in Ref. 4.

Each of the three methods of testing has inherent limitations. In selecting the method to use for a particular testing application, the potential sources of error must be recognized so that steps can be taken to minimize their effects on the test results. The potential sources of error in simulating boundary conditions for the three types of simulation methods are given in Tables 3-1, 3-2, and 3-3. Only the sources of error that are attributable to the energy sources are listed; other sources that must be considered when analyzing test data are those associated with uncertainties in boundary-condition specification (i.e., errors in specification of desired surface temperature, absorbed heat fluxes, and solar spectral energy distribution). Numerical evaluation of the magnitude of the errors will be accomplished during the last phase of the program.

3.2 SOURCE CHARACTERISTICS

A major task in establishing a set of specifications for thermal-vacuum testing of the spacecraft is the selection of an appropriate source of thermal energy. An investigation of various types of energy sources was initiated during this phase of the program. The effort to date has consisted of (1) defining the characteristics that must be considered in selecting the type of source to be used and (2) gathering information on various types of solar simulator and infrared sources.

Characteristics that are considered important in selecting an energy source for environmental testing are listed in Table 3-4. Tables 3-5 and 3-6 provide some of these characteristics for three different types of compact arc lamps.

Recent data on experimental compact arc lamps show that sources are available which have a brightness greater than that of the sun's average brightness outside the atmosphere; for example, data from Ref. 5 on a fluid transpiration arc lamp indicate an

Table 3-1

POTENTIAL ERRORS ATTRIBUTABLE TO ENERGY SOURCE
CHARACTERISTICS FOR SURFACE TEMPERATURE SIMULATION

- Local nonuniformities in simulated surface temperature distribution
- Errors in measurement of surface temperature
- Changes in effective spacecraft surface emittance incurred when strip heaters or heater blankets are used
- Reduction in view factor between spacecraft surface and vacuum chamber cold walls when infrared lamps are used

Table 3-2

POTENTIAL ERRORS ATTRIBUTABLE TO ENERGY SOURCE
CHARACTERISTICS FOR ABSORBED HEAT FLUX SIMULATION

- Errors in measurement of optical properties of spacecraft outer surface
- Errors in measurement control of spectral energy output of energy source
- Accuracy of calculation of absorbed heat flux as a function of inputs to the energy source (analytical determination of view factors to energy source, etc.)
- Reflection of energy from cold walls
- Thermal radiation interchange between spacecraft and energy sources
- Reduction in view factor between spacecraft surface and vacuum chamber cold wall due to interposition of energy source between spacecraft and cold walls
- Errors due to geometrical nonuniformities or irregularities in energy source output
- Errors due to inability to match absorbed heat fluxes on surfaces which have different infrared absorptance and are illuminated by the same source
- Errors due to changes in surface optical properties during testing

Table 3-3

POTENTIAL ERRORS ATTRIBUTABLE TO ENERGY SOURCE
CHARACTERISTICS FOR SOLAR SPECTRAL ENERGY SIMULATION

- Deviations of spectral intensity of source from the solar spectrum (spectral mismatch)
- Imperfect source beam collimation
- Spatial nonuniformities in source output
- Errors in measurement of spectral energy output of source
- Interreflections between source and the spacecraft
- Extraneous source energy reflection from nonblack cold walls
- Reduction in view factor between spacecraft and cold walls due to interposition of source
- Overlapping of radiation fields from adjacent sources
- Errors due to filter degradation during testing

Table 3-4

CHARACTERISTICS TO BE CONSIDERED IN SELECTION
OF ENERGY SOURCE

- Maximum radiant flux attainable
- Spatial distribution of radiant intensity
- Spatial and temporal uniformity of flux at test section
- Maximum size of test section
- Spectral distribution of radiant flux
- Effect on total heat balance (collimation, blockage of view of cold walls, etc.)
- Reliability and source life
- Cost of installation and operation
- Variation in radiant intensity with changes in input power
- Operational requirements (cooling of reflectors, effect of operation in vacuum, etc.)

Table 3-5

MAIN DATA OF HIGH WATTAGE XENON, MERCURY, AND
MERCURY-XENON COMPACT ARC LAMPS(a)

No.	Lamp Wattage (W)	Type Designation	Gas/Vapor Filling	Max. Bulb Outer Diameter (mm)	Max. Overall Length (in.)	Arc Length in Operation (mm)	Internal Operating Pressure (atm)	Lamp Operating Voltage (V)	Lamp Operating Current
1	800 ac	SAH800C ^(b)	Hg	42	9-1/2	8.5	10	70	12
2	900 dc	XB0900W ^(c)	Xenon	40	12-13/16	3.4		22	42
3	1,000 dc	528B ^(d)	Hg-Xenon	45	7	6.5		65	16
4	1,000 ac	SAH1,000A ^(b)	Hg	51	9-1/2	6.5	25	65	18
5	1,000 ac	SAHX1,000A ^(b)	Hg-Xenon	51	9-1/2	6.5	30	65	18
6	1,600 dc	XB01,600W ^(c)	Xenon	52	14-9/16	4.2		26	63
7	2,000 dc	UXL2,000DK ^(e)	Xenon	53	14-3/16	6		28	70
8	2,000 dc	XE2,000 ^(f)	Xenon	54	14-13/16	3.5		22.3	90
9	2,200 dc	491C ^(d)	Xenon	57	12-1/2	4	16	20-23	100
10	2,500 dc	929B ^(d)	Hg-Xenon	64	12-1/2	4	18	45-55	50
11	2,500 ac	SAH2,500A ^(b)	Hg	70	13	10	15	65	45
12	2,500 ac	SAHX2,500A ^(b)	Hg-Xenon	70	13	10	20	65	45
13	2,500 dc	SAHX2,500B ^(b)	Hg-Xenon	70	13	4.5	30	50	50
14	2,500 dc	XB02,500W ^(c)	Xenon	57	16-7/8	6.2		30.1	83
15	4,000 dc	UXL4,000DK ^(e)	Xenon		15-3/4	7		33	120
16	5,000 dc ^(g)	932B ^(d)	Hg-Xenon	86	13-1/2	5	15	30-60	100
17	5,000 dc	K35,000 ^(f)	Xenon	89	19-1/2	7		34.5	145
18	10,000 dc	XE10,000 ^(h)	Xenon	92	27-1/2	8	10	40	250
19	20,000 dc ^(g)	XE20,000 ^(h)	Xenon	120	33-1/2	13.5	6	50	400

(a) Reproduced from Ref. 7.

(b) Westinghouse, U. S. A.

(c) Osram, West Germany.

(d) Hasovia, U. S. A.

(e) Ushie Kogyo Katsusha, Japan.

(f) General Electric, U. S. A.

(g) Experimental lamp.

(h) Daro-Tem, U. S. A.

Table 3-6

MAIN DATA OF HIGH WATTAGE XENON, MERCURY, AND
MERCURY-XENON COMPACT ARC LAMPS(a)

No.	Lamp Wattage (W)	Type Designation	Gas/Vapor Filling	Brightness Data (cd/mm ²)(b)			Initial Lumens	Initial Efficiency (lm/W)	Rated Life (hr)
				Peak	Average for Arc Area	Arc Area Width and Length (mm)			
1	800 ac	SAH800C(c)	Hg	180			40,000	50	600
2	900 dc	XB0900W(d)	Xenon		380	1.7 × 3.4	30,500	34	2,000
3	1,000 dc	528B(e)	Hg-Xenon	970	230	2.5 × 6.5	52,000	52	1,000(f)
4	1,000 ac	SAH1,000A(c)	Hg	475			50,000	50	300(g)
5	1,000 ac	SAHX1,000A(c)	Hg-Xenon	475			50,000	50	400(g)
6	1,600 dc	XB01,600W(d)	Xenon		430	2.1 × 4.2	56,000	35	2,000
7	2,000 dc	UXL2,000DK(h)	Xenon		550	2 × 6	70,000	35	
8	2,000 dc	XE2,000(i)	Xenon	4,100	820	3 × 3	85,000	42.5	500(j)
9	2,200 dc	491C(e)	Xenon	3,300	440	2.3 × 4	75,000	34	1,000(f)
10	2,500 dc	929B(e)	Hg-Xenon	2,050	540	2.5 × 4	120,000	48	1,000(f)
11	2,500 ac	SAH2,500A(c)	Hg	325			125,000	50	400(g)
12	2,500 ac	SAHX2,500A(c)	Hg-Xenon	325			125,000	50	200(g)
13	2,500 dc	SAHX2,500B(c)	Hg-Xenon	2,050			120,000	48	400(g)
14	2,500 dc	XB02,500W(d)	Xenon		450	3.1 × 6.2	100,000	40	1,500
15	4,000 dc	UXL4,000DK(h)	Xenon		600	3 × 7	120,000	30	
16	5,000 dc(k)	932B(e)	Hg-Xenon	2,250	780	3 × 5	230,000	46	
17	5,000 dc	X35,000(i)	Xenon	5,900	870	5 × 5	275,000	55	500(j)
18	10,000 dc	XE10,000(h)	Xenon	9,500	1,250	5 × 5	480,000	48	500(j)
19	20,000 dc(k)	XE20,000(l)	Xenon	7,500	1,700	5 × 5	1,000,000	50	

(g) In vertical position 8 hr per start.

(h) Ushie Kegyo Katsha, Japan.

(i) General Electric, U.S.A.

(j) Preliminary data.

(k) Experimental lamp.

(l) Daro-Tem, U.S.A.

(a) Reproduced from Ref. 7.

(b) Average brightness of Sun outside Earth's atmosphere = 1653 cd/mm².

(c) Westinghouse, U.S.A.

(d) Osram West Germany.

(e) Hasovia, U.S.A.

(f) 12 hr per start.

attainable source brightness of $2.69 \times 10^7 \text{ W/m}^2\text{-sr}$, a value approximately 30 percent greater than that of the sun. Such data are not particularly meaningful, however, unless they are related to a specific spatial distribution of radiant intensity. Variations in the spatial distribution of intensity of a tubular quartz envelope tungsten filament lamp with various reflectors are illustrated in Figs. 3-1 and 3-2. The effect of various polar intensity distributions on a cylindrical surface has been analyzed for three assumed intensity distributions. The results of this analysis, presented in Appendix C, indicate that it is possible to provide a lamp array (assuming discrete line sources) which will provide a fairly uniform distribution of incident flux on a cylindrical surface.

An estimate of the effect of solar simulation source deviations from the true solar spectrum has been made for two materials contemplated for use on solar probe spacecraft. Figures 3-3 and 3-4 give spectral reflectance values for two types of Optical Solar Reflectors and filtered silicon solar cells. Using the data given in Fig. 3-3 and a band energy approximation to the absorbed energy distribution, calculations of total absorbed energy and effective absorptance of these materials were made for exposure to the sun, an argon-filled fluid transpiration arc source operating at 200 psi, and a carbon arc source. The results of these calculations are shown in Tables 3-7 and 3-8.* In these calculations the spectral output of the argon and carbon arc sources has been normalized to provide a total radiated intensity equal to that of the sun. The most significant result is the ratio of total absorptance of source radiation to total absorptance of solar radiation, α_s/α_o . For a source with total radiated intensity equal to that of the sun, a heat balance on the spacecraft yields

$$\frac{\epsilon A_v (T_v^4 - T_s^4)}{\alpha_o A} = \frac{\epsilon_s A_v (T_{vs}^4 - T_w^4)}{\alpha_s A}$$

*Similar information for the OSR and solar cell materials shown in Fig. 3-4 will be provided in the final report of this program.

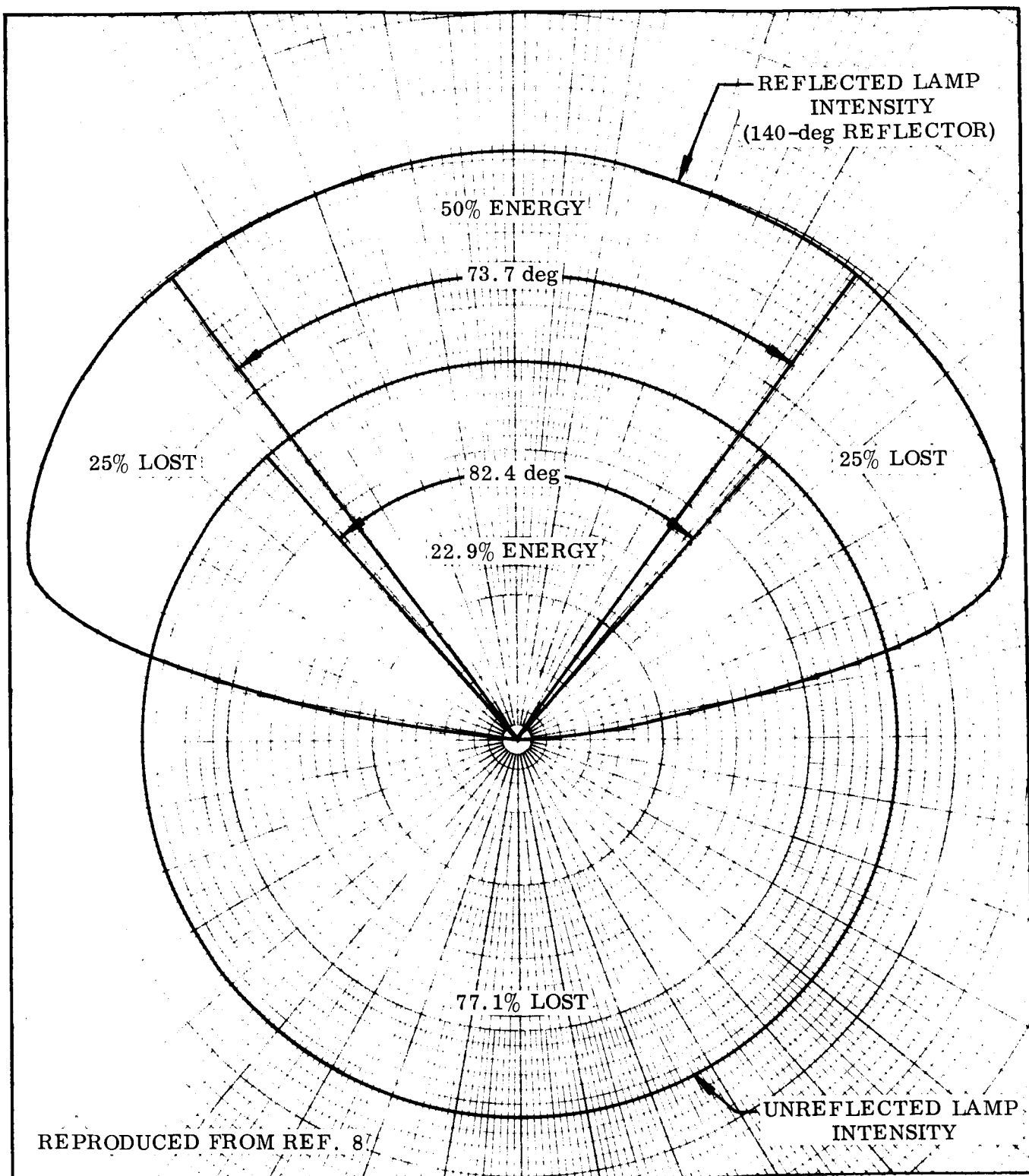


Fig. 3-1 Directional Intensity Variation of Reflected and Unreflected Tubular Quartz Envelope Tungsten Filament Lamp

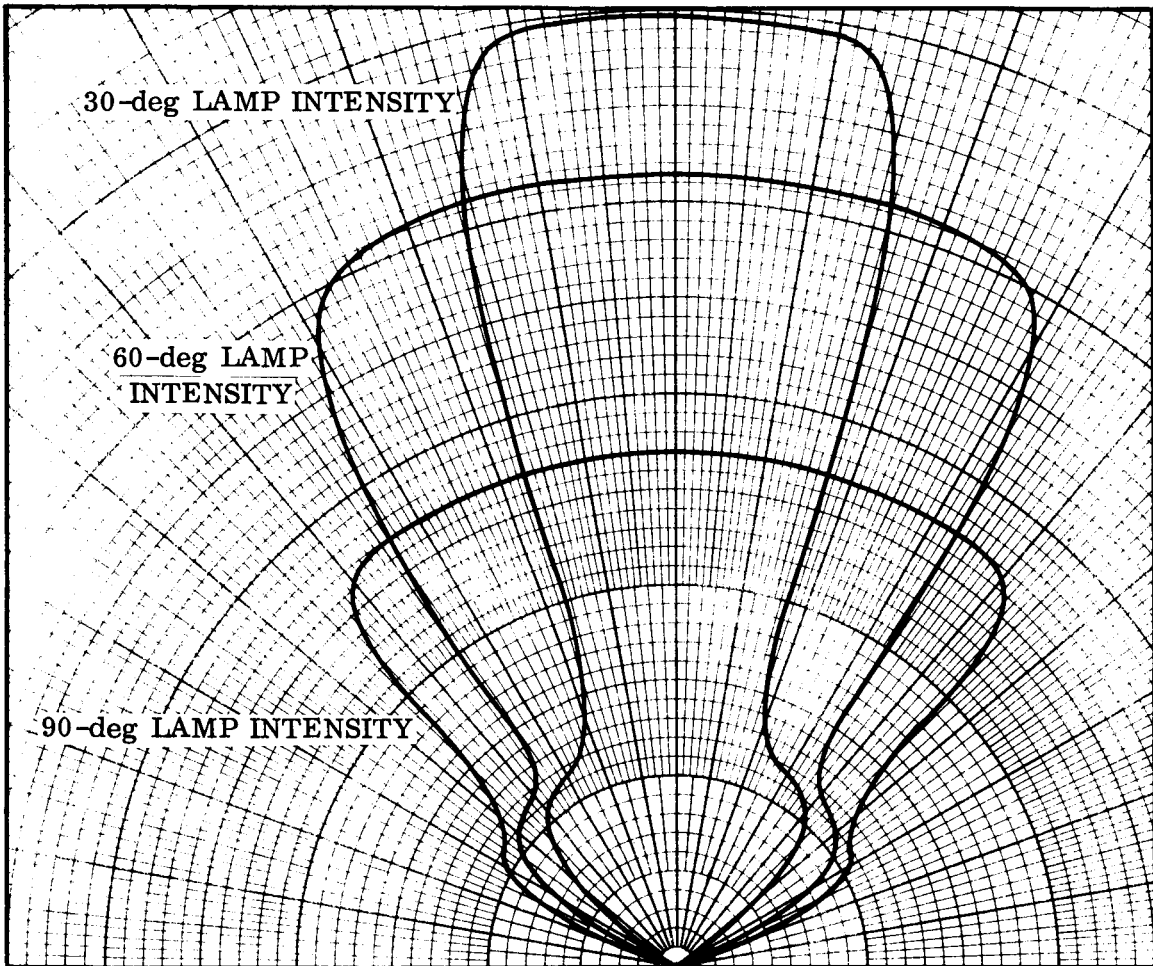


Fig. 3-2 Directional Radiation Properties, Reflected Lamps

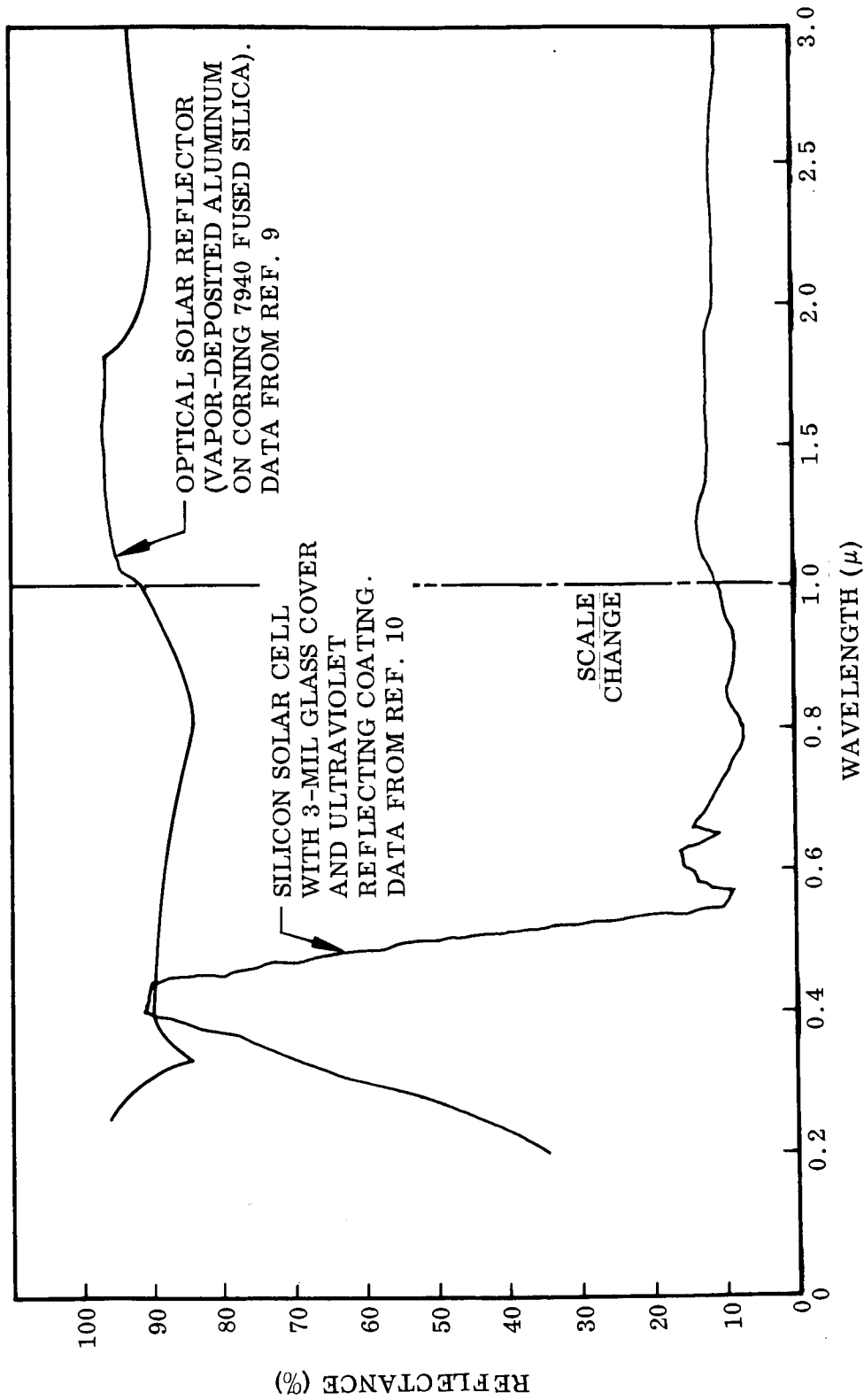


Fig. 3-3 Spectral Reflectance of Spacecraft Materials

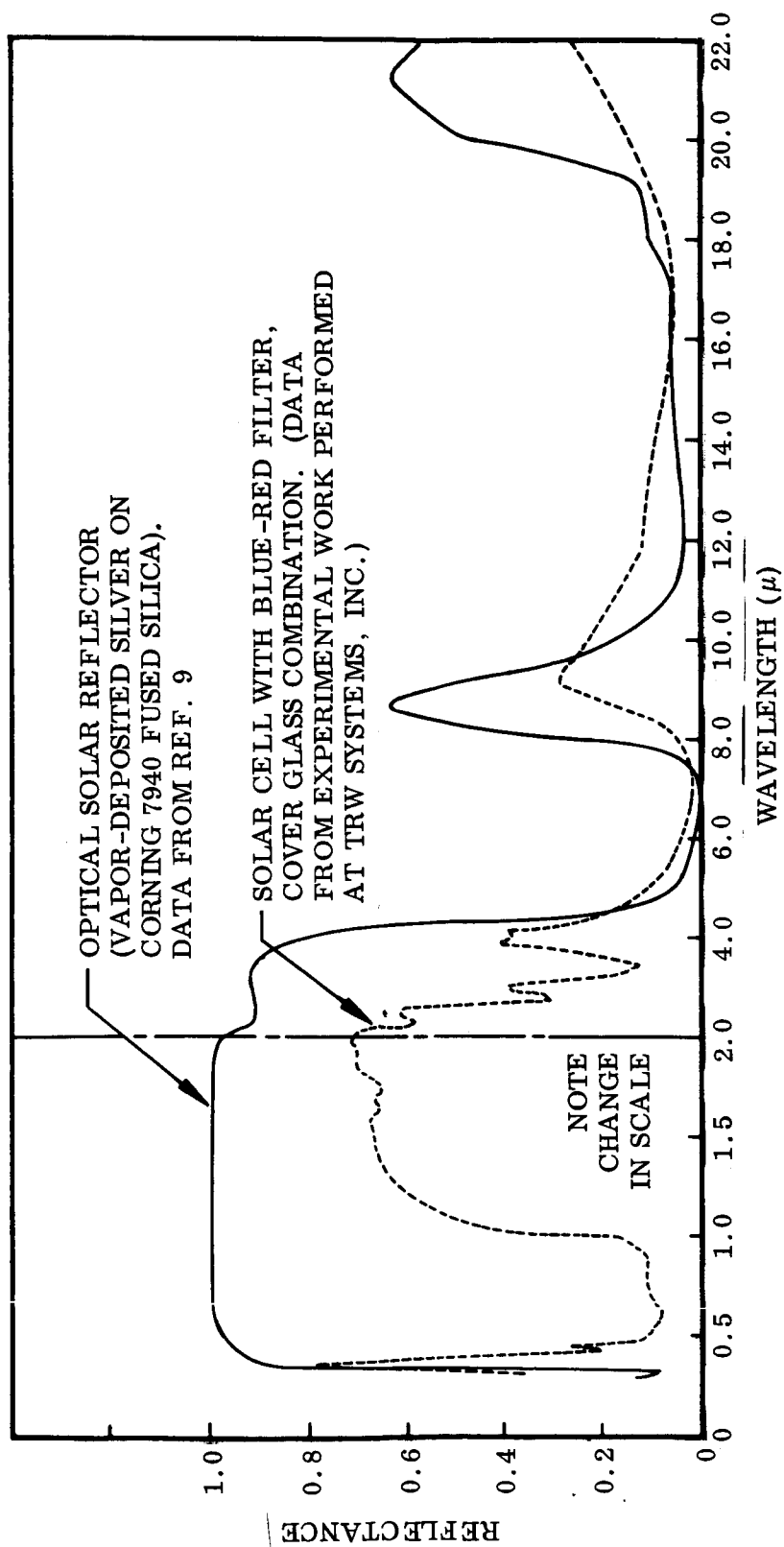


Fig. 3-4 Spectral Reflectance of Spacecraft Materials

Table 3-7
ENERGY ABSORPTION DATA - SILICON SOLAR CELL

$\Delta\lambda$	α_λ	Absorbed Energy Comparison Values are for Silicon Solar-Cell Data Given in Fig. 3-3					
		Incident Solar	Energy Absorbed	Incident Argon	Energy Absorbed	Incident Carbon Arc	Energy Absorbed
0.20-0.30	0.55	17.2	9.5	22.6	12.4	18.2	10.0
0.30-0.36	0.32	59.2	18.9	74.5	23.8	77.0	24.6
0.36-0.42	0.13	87.1	11.3	130.2	16.9	210.0	27.3
0.42-0.46	0.14	79.4	11.1	105.1	14.7	133.0	18.6
0.46-0.50	0.34	84.4	28.7	102.3	34.8	119.0	40.5
0.50-0.54	0.70	78.2	54.7	99.9	69.9	107.8	75.5
0.54-0.58	0.88	77.6	68.3	83.6	73.6	95.2	83.8
0.58-0.62	0.85	73.9	62.8	71.3	60.6	81.2	69.0
0.62-0.66	0.87	68.6	59.7	50.4	43.8	70.0	60.9
0.66-0.70	0.87	62.5	54.5	41.0	35.7	54.6	47.5
0.70-0.76	0.90	85.0	76.5	127.8	115.0	58.8	52.9
0.76-0.82	0.92	73.8	67.9	149.3	137.4	42.0	38.6
0.82-0.90	0.915	83.8	76.7	125.4	114.7	43.4	38.7
0.90-1.00	0.91	84.5	76.9	35.4	32.2	51.8	47.1
1.00-1.10	0.88	66.5	58.5	17.8	15.7	37.8	33.3
1.10-1.30	0.87	95.5	83.1	49.3	42.9	57.4	49.9
1.30-1.60	0.88	84.6	74.4	68.1	59.9	47.6	41.9
1.60-2.30	0.885	82.6	73.1	40.4	35.8	70.0	62.0
2.30-3.00	0.895	55.6	49.8	6.4	5.7	25.2	22.6
Total Energy, W/m ²		1400.0	1016.3	1400.8	935.5	1400.0	844.7
Total Absorptance		0.726		0.668		0.603	
α_s/α_o		1.00		0.92		0.83	

Table 3-8
ENERGY ABSORPTION DATA - OPTICAL SOLAR REFLECTANCE

$\Delta\lambda$	α_λ	Absorbed Energy Comparison Values are for Vacuum Deposited Aluminum Optical Solar Reflector (Fig. 3-3)					
		Incident Solar	Energy Absorbed	Incident Argon	Energy Absorbed	Incident Carbon Arc	Energy Absorbed
0.20-0.30	0.07	17.2	1.2	22.6	1.6	18.2	1.3
0.30-0.36	0.13	59.2	7.7	74.5	9.7	77.0	10.0
0.36-0.42	0.11	87.1	9.6	130.2	14.3	210.0	23.1
0.42-0.46	0.105	79.4	8.3	105.1	11.0	133.0	14.0
0.46-0.50	0.107	84.4	9.0	102.3	10.9	119.0	12.7
0.50-0.54	0.11	78.2	8.6	99.9	11.0	107.8	18.9
0.54-0.58	0.114	77.6	8.8	83.6	9.5	95.2	10.9
0.58-0.62	0.118	73.9	8.7	71.3	8.4	81.2	9.6
0.62-0.66	0.124	68.6	8.5	50.4	6.2	70.0	8.7
0.66-0.70	0.13	62.3	8.1	41.0	5.3	54.6	7.1
0.70-0.76	0.14	85.0	11.9	127.8	17.9	58.8	8.2
0.76-0.82	0.155	73.8	11.4	149.3	23.1	42.0	6.5
0.82-0.90	0.15	83.8	12.6	125.4	18.8	43.4	6.5
0.90-1.00	0.115	84.5	9.7	35.4	4.1	51.8	6.0
1.00-1.10	0.07	66.5	4.7	17.8	1.2	37.8	2.6
1.10-1.30	0.05	95.5	4.8	49.3	2.5	57.4	2.9
1.30-1.60	0.04	84.6	3.4	68.1	2.7	47.6	1.9
1.60-2.30	0.07	82.6	5.8	40.4	2.8	70.0	4.9
2.30-3.00	0.08	55.6	4.4	6.4	0.5	25.2	2.0
Total Energy, W/m ²		1400.0	147.2	1400.8	161.5	1400.0	157.8
Total Absorptance		0.105		0.115		0.113	
α_s/α_o		1.00		1.095		1.076	

Assuming that $T_s = T_{\text{space}} = 0^\circ \text{K}$, and $\epsilon = \epsilon_s$,

$$T_{\text{VS}}^4 = (\alpha_s/\alpha_o) T_v^4 + T_w^4$$

For various values of the dependent variables α_s/α_o and T_v , the equilibrium temperature error $T = T_{\text{VS}} - T_v$ has been calculated in Ref. 6 and is shown graphically in Fig. 3-5. For a vehicle equilibrium temperature of 300°K (70°F), the errors in equilibrium temperature which would be incurred for the fluid transpiration arc and carbon arc sources are shown in Table 3-9.

Table 3-9
TEMPERATURE ERRORS FOR ARGON AND
CARBON ARC SOURCES

Material	Temperature Error			
	Argon Arc		Carbon Arc	
	(%)	(° F)	(%)	(° F)
Silicon Solar Cell (Fig. 3-3)	-2	-11	-4.3	-23
OSR (Fig. 3-3)	+3	+16	+2	+11

Thus, in the case of carbon arc solar simulation, a maximum temperature error of 23°F is possible with a solar cell covered spacecraft; these results indicate the care that is required to match total heat flux inputs even when "solar simulation" facilities are used. Calculations of direct and reflected simulated solar heat inputs are, therefore, a necessary step in both the evaluation of solar simulation facilities and absorbed heat flux simulation facilities.

Investigations of energy source characteristics will continue during the next phase of the program. The final report will include a comprehensive presentation of characteristics for all the sources studied, including representative spectral energy distribution curves for each source.

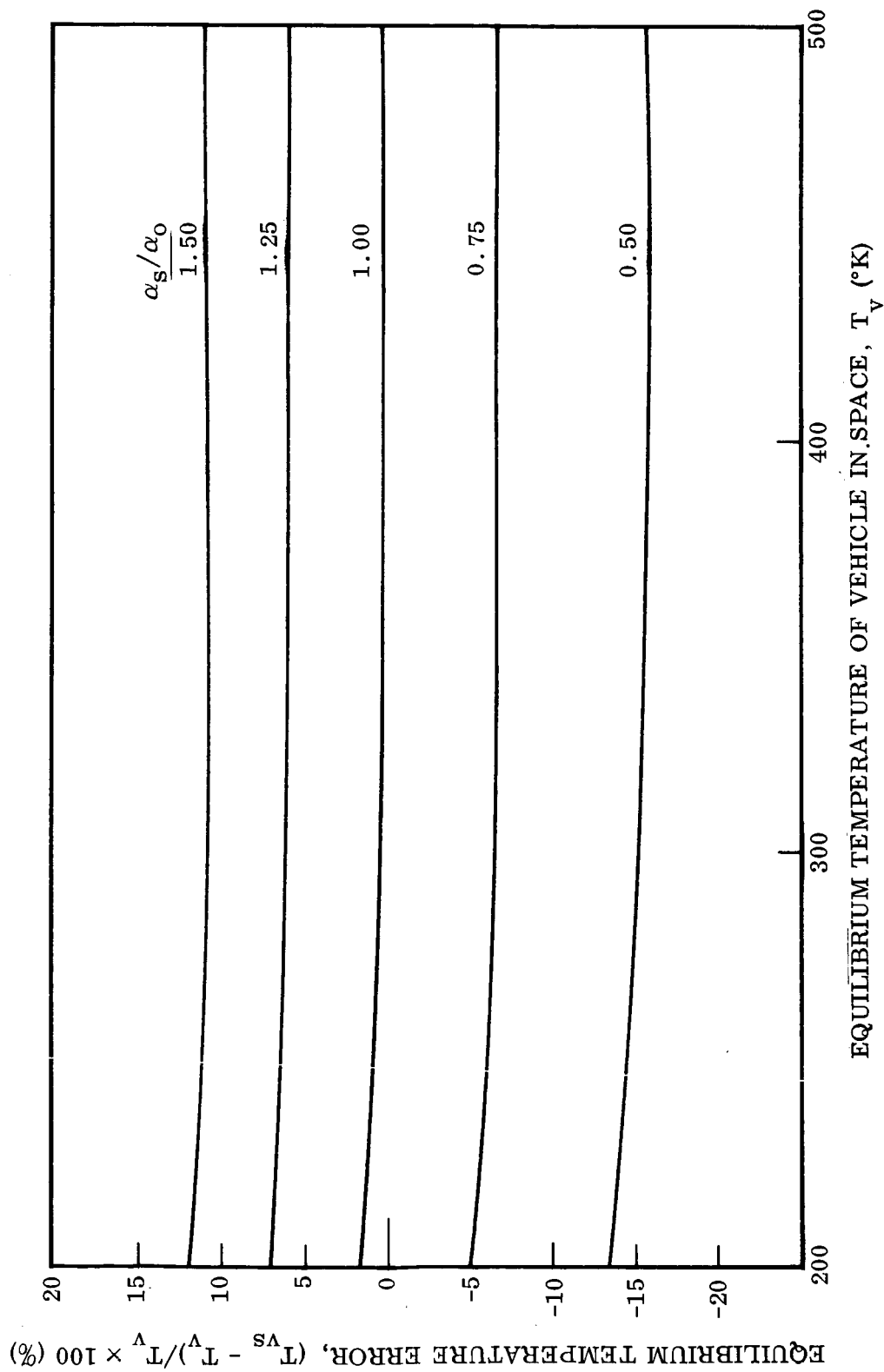


Fig. 3-5 Error in Equilibrium Temperature for Constant Simulator Output

Section 4

FUTURE WORK

The following sections describe work which is planned (or in progress) to accomplish the program objectives.

4.1 LABORATORY INVESTIGATIONS - THERMAL MODELING

A physical thermal test model of the spacecraft will be designed, fabricated, and tested under controlled thermal and vacuum conditions. It is contemplated that the model will be approximately half the size of the actual spacecraft. Accepted thermal modeling techniques will be employed in the design and fabrication of the scaled-down model. The model will be designed such that its thermal performance will closely match that of the thermal analyzer model described in Appendix A. No attempt will be made to duplicate physical characteristics of the vehicle, except that superinsulation and the Optical Solar Reflector thermal control surface will be used in their applicable locations. The primary purpose of constructing and testing the test model is to evaluate the ability of the computer thermal analyzer model to predict the thermal behavior of the spacecraft at high solar intensities.

Confirmation of thermal similarity between the physical model and thermal analyzer model will be accomplished by subjecting the model under vacuum conditions to a solar intensity of 1-sun A. U. using a carbon arc energy source. Where dissimilarities occur, the thermal analyzer model will be altered to match the test model. Testing of the model will then be accomplished at various intensities between 1 and 25 suns, employing a bank of tungsten lamps as the energy source. Test results will be compared with results obtained from additional computer runs of the thermal analyzer model.

4.2 TEST SPECIFICATIONS

The work reported in Section 3 will be extended to provide detailed test specifications for thermal evaluation testing of the spacecraft. This will be accomplished by further compilation of information on characteristics of heat flux and solar simulation sources and establishment of the combinations of test setups and special test techniques that appear to be most desirable. Using these results, and supporting computer analyses as required, a tradeoff study of the various test techniques will be performed on the basis of accuracy of simulation, the effect of inaccuracies on heat flux absorbed and internal spacecraft temperatures, relative reliability, cost, and other factors which influence the choice of a simulation system.

Calculations of spacecraft outer shell temperatures and absorbed heat flux will be performed by hand for the contemplated test arrangements. However, the effect of deviations in externally absorbed heat flux from those experienced in the true space environment on internal component temperatures may be accurately determined only by computer analysis. In addition, the magnitude of effects of radiative interchange between the vehicle outer shell and energy sources and vacuum chamber cold walls may require computer analysis for their determination. The extent to which these analyses are pursued by computer techniques will be determined by the estimated adequacy of hand-calculated estimates in evaluating candidate facility requirements.

Section 5

CONCLUSIONS

Results of the thermal analysis of two proposed spacecraft configurations have provided basic computer models with which predictions of variations in spacecraft temperatures may be made as a function of externally imposed heat fluxes. These models may be used to estimate temperature errors incurred in various types of environmental simulation facilities. Through necessity, the thermal analyzer models were designed to be relatively simple and yet maintain some degree of reality so that calculated temperatures could be compared with temperatures obtained from flight and laboratory tests. Work to be accomplished during the remaining portions of the program, involving testing of a physical thermal model under controlled thermal-vacuum conditions, will determine whether a more detailed thermal analyzer model should be designed.

Temperature distributions within the two configurations were determined for spacecraft-to-solar distances of 0.2 and 1.0 A. U. The results indicate that instrument platform temperatures can be maintained at acceptable levels for both distances as long as a high thermal resistance is provided between the upper solar cell array and the sun-sensor brackets. The thermal analysis also indicated that instrument platform temperatures are relatively insensitive to slight variations in multilayer insulation thermal conductivity.

Energy source characteristics were determined for a limited number of sources, and a preliminary estimate of temperature errors due to spectral mismatch between solar simulation sources and the spectral energy distribution of the sun was made. Results show that spectral dissimilarities in energy distribution can cause large variations between temperatures predicted for a vehicle in space and temperatures observed during laboratory testing. Therefore, it is necessary to match carefully the predicted

total heat flux inputs during laboratory thermal testing. Work is continuing toward a more detailed estimate of the adequacy of the candidate simulation methods discussed in Section 3, as well as measurement of additional lamp spectral output data and investigation of the applicability of thermal scale modeling to environmental testing of spacecraft at high solar intensities.

Section 6
REFERENCES

1. F. S. Johnson, "The Solar Constant," J. Meteorol., Vol. II, 1959, pp. 431-439
2. A. Charnes and S. Raynor, "Solar Heating of a Rotating, Cylindrical Space Vehicle," ARS J., Vol. 30, 1960, pp. 479-484
3. I. B. Irving and W. J. Billerbeck, Thermal Problems Involved in Space Simulation, TG-595, The Johns Hopkins University, Applied Physics Laboratory, Silver Spring, Md., Aug 1964
4. J. W. Anderson, E. A. LaBlanc, and M. McNally, "Space Thermal Simulation, Without a Solar Simulator," Proc. Int. Symposium on Solar Radiation Simulation, Los Angeles, Calif., 18-20 Jan 1965
5. W. A. Jaatinen, E. A. Mayer, and F. R. Sileo, "New Approaches to Sources for Solar Simulation," Proc. Int. Symposium on Solar Radiation Simulation, Los Angeles, Calif., 18-20 Jan 1965
6. G. MacFarlane, "Is Spectral Match Really Necessary?" Proc. Int. Symposium on Solar Radiation Simulation, Los Angeles, Calif., 18-20 Jan 1965
7. T. K. Pugmire and R. W. Liebermann, Final Report - Radiant Heating Simulation, NASA CR-65023, 3 May 1965
8. "Dynamic Radiant Heating Applications," Bulletin 504.21, Research, Inc., Controls Division, Minneapolis, Minn.
9. K. N. Marshall and R. L. Olson, Optical Solar Reflector Thermal Control Surface, LMSC 3-56-65-2, Lockheed Missiles & Space Company, Palo Alto, Calif., 2 Feb 1965
10. D. K. Edwards, "Directional Solar Reflectances in the Space Vehicle Temperature Control Problem," ARS J., Nov 1961, pp. 1548-1553

11. Thermal Analyzer Control System for IBM 709-7090-7094 Computer Engineering Utilization Manual, LMSC 3-56-65-8, Lockheed Missiles & Space Company, Sunnyvale, Calif., 1 Sep 1965
12. R. P. Bobco and T. Ishimoto, "Temperature Errors in Simple Systems Caused by Deviations From Ideal Space - Solar Simulation," Proc. Int. Symposium on Solar Radiation Simulation, Los Angeles, Calif., 18-20 Jan 1965
13. N. C. Latture, "Experimental Correlation Between Heat Flux and Solar Irradiated Surfaces," Proc. Int. Symposium on Solar Radiation Simulation, Los Angeles, Calif., 18-20 Jan 1965
14. A. J. Drummond, "The Extraterrestrial Solar Constant," Proc. Int. Symposium on Solar Radiation Simulation, Los Angeles, Calif., 18-20 Jan 1965

Appendix A

DETAILED DESCRIPTION OF THERMAL ANALYZER PROGRAM

A.1 GENERAL CHARACTERISTICS

The Mark-5C Thermal Analyzer Program (Ref. 11) solves transient and steady-state heat flow problems using the digital computer to obtain a finite difference solution for the analogous R-C electrical network. It can be programmed to run parametric studies and will handle periodic and continuous functions. The input capacity of the program is approximately 18,000 words. This means that thermal networks of 1,000 nodes can be handled with ease; 3,000-node networks have been run successfully. Steady-state analyses of the solar-powered and RTG-powered vehicle configurations were performed utilizing the Mark-5C Thermal Analyzer Program and the IBM-7940 digital computer.

The thermal model for the solar-powered configuration was developed with the following characteristics:

- (1) 43 nodes (see Fig. A-1)
- (2) 55 conduction resistors
- (3) 64 radiation resistors
 - (a) 24 radiation-to-space resistors
 - (b) 40 component-to-component radiation resistors
 - (c) 4 radiation constants associated with the lower instrument platform and louver surface
- (4) 21 heat rates introduced into the analog network
 - (a) 5 constant internal heat rates
 - (b) 16 variable external heat rates corresponding to solar distance

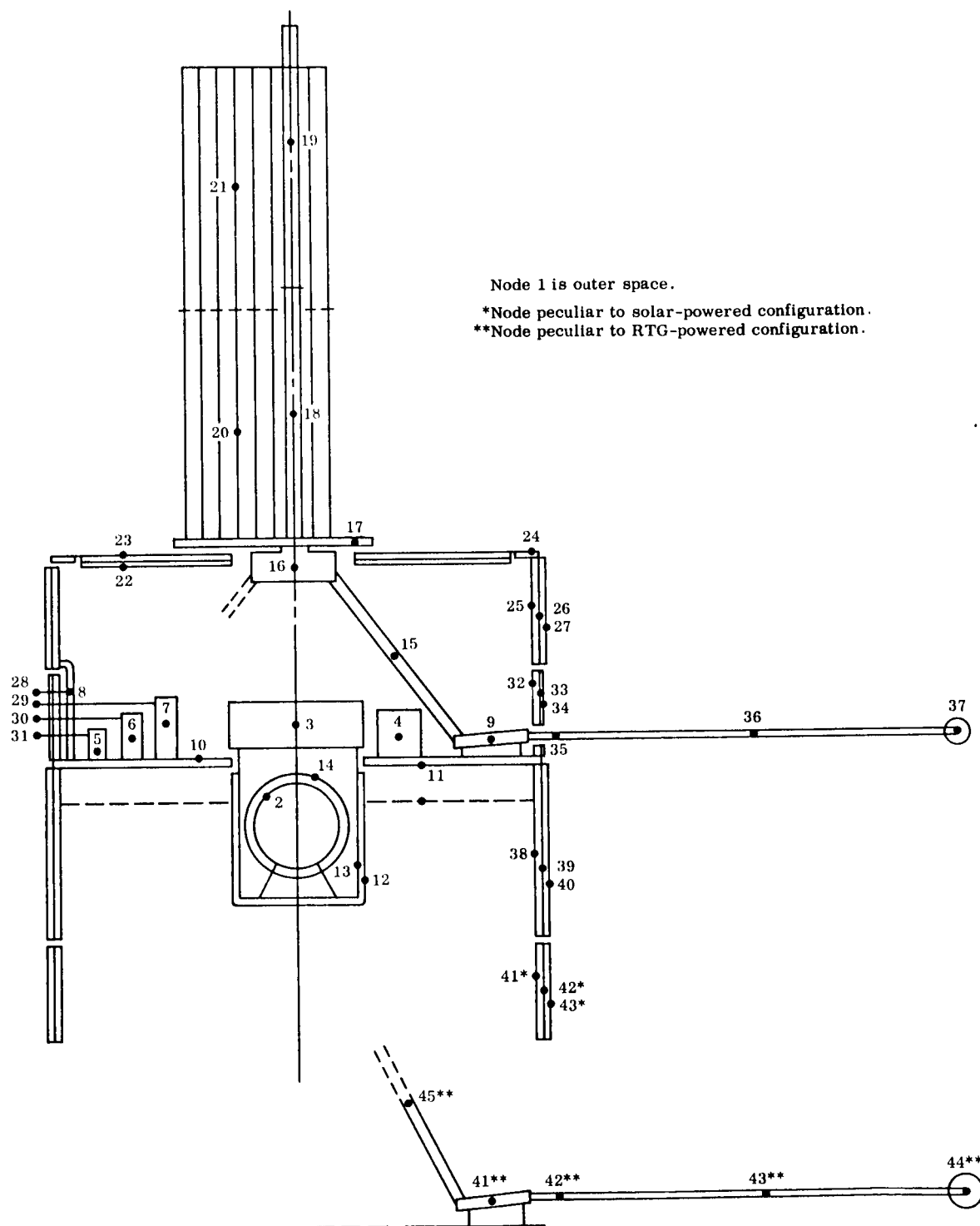


Fig. A-1 Thermal Analyzer Model Node Locations

A-2

LOCKHEED PALO ALTO RESEARCH LABORATORY
 LOCKHEED MISSILES & SPACE COMPANY
 A GROUP DIVISION OF LOCKHEED AIRCRAFT CORPORATION

The thermal model for the RTG-powered configuration was developed with the following characteristics:

- (1) 45 nodes (see Fig. A-1)
- (2) 56 conduction resistors
- (3) 70 radiation resistors
 - (a) 25 radiation-to-space resistors
 - (b) 45 component-to-component radiation resistors
 - (c) 3 radiation constants associated with the lower instrument platform and louver surface
- (4) 24 heat rates introduced into the analog network
 - (a) 6 constant internal heat rates
 - (b) 18 variable external heat rates corresponding to solar distance

A.2 HEAT RATE COMPUTATION

A.2.1 Solar Energy

Solar heat rates for continuously illuminated surfaces at 1 A. U. were calculated using the relation

$$Q \left(\frac{\text{Btu}}{\text{sec}} \right) = \alpha_s A_p (\text{in.}^2) 0.856 \times 10^{-3} \left(\frac{\text{Btu}}{\text{sec-in.}^2} \right) \quad (\text{A. 1})$$

For plane, or nearly plane, surfaces rotating at a constant rate with respect to the vehicle-sun line, solar heat rates at 1 A. U. were found using the relation

$$Q \left(\frac{\text{Btu}}{\text{sec}} \right) = \alpha_s \frac{A_p}{\pi} (\text{in.}^2) 0.856 \times 10^{-3} \left(\frac{\text{Btu}}{\text{sec-in.}^2} \right) \quad (\text{A. 2})$$

Solar heat rates for 0.2 A. U. were calculated by multiplying the heat rates found at 1 A. U. by $(1/0.2)^2 = 25$. Determination of solar heat rates into the lower solar

cell array was unnecessary for the solar-powered configuration at 0.2 A. U. , since the despun shield controls the array temperature to a maximum value of 190° F. The 0.2 A. U. heat rates into the experiment apertures were reduced to the 1 A. U. level because of the variable shutter system to be employed.

Solar heat rates for the solar-powered and RTG-powered configurations are given in Tables A-1 and A-2, respectively.

A. 2. 2 Internal Power

Power dissipation from sources internal to the vehicle is given in Table A-3. The equipment shown is common to both vehicle configurations analyzed, with the exception of the two RTG power units (node 44) which apply only to the RTG-powered configuration.

A. 3 ENERGY EXCHANGE BY CONDUCTION

One-dimensional conduction resistance between the various nodes was either estimated using best engineering judgment where details of vehicle configuration were unavailable or calculated where possible using the relation

$$R_{ij} \left(\frac{\text{sec-}^\circ\text{F}}{\text{Btu}} \right) = \frac{L(\text{in.})}{k \left(\frac{\text{Btu}}{\text{hr-ft-}^\circ\text{F}} \right) A(\text{in.}^2)} \times 4.32 \times 10^4 \left(\frac{\text{sec-in.}}{\text{hr-ft}} \right) \quad (\text{A. 3})$$

In cases where conductive resistances were found to be less than 100 sec-° F/Btu , a value of 100 sec-° F/Btu was used in the computer calculation. Excessive computer calculation time is avoided by using a value such as this for conduction resistance, and experience has shown that no significant error results in the final equilibrium temperatures.

A relation for heat conduction parallel to the facing sheets in the honeycomb structure was developed from honeycomb geometry. For 1/4-in. aluminum honeycomb with

Table A-1
SOLAR HEAT RATES TO EXTERNAL SURFACES AT 1 A.U., SOLAR-POWERED CONFIGURATION

Description	Node	Projected Area, A_p (in. ²)	α_s	Heat Rate Relation Used	Heat Rate (Btu/sec)	Comments
Dipole Antenna and Reflector	17	24	0.08	A-1	0.165×10^{-2}	OSR surfaces degraded from $\alpha_s = 0.04$ to 0.08 due to curvature of surfaces
	18	52	0.08		0.356×10^{-2}	
	19	52	0.08		0.356×10^{-2}	
Solar-Cell Arrays	20	152	0.25	A-1	0.325×10^{-1}	White paint on reflector section of antenna
	21	152	0.25		0.325×10^{-1}	
	27	298	0.69		1.760×10^{-1}	
OSR Band	40	522	0.69	A-1	3.080×10^{-1}	Three booms combined and divided into three radial lengths with OSR surfaces degraded from $\alpha_s = 0.04$ to 0.08 due to curvature of surfaces
	43	280	0.69		1.650×10^{-1}	
	34	208	0.04		0.712×10^{-2}	
Booms	35	40.5	0.08	A-2	0.880×10^{-3}	White paint with holes
	36	80.5	0.08		0.590×10^{-3}	
	37	120.0	0.08		1.760×10^{-3}	
Five Sun Sensors	28	20.75	0.4	A-2	0.226×10^{-2}	OSR with holes
Experiment No. 4 and No. 6	29	11.20	0.1	A-2	0.305×10^{-3}	
Experiment No. 7	30	0.65	1.0	A-2	1.750×10^{-4}	Opening assumed to be blackbody
Experiment No. 2	31	14.10	0.5	A-2	1.920×10^{-3}	Aluminum with holes

Table A-2
SOLAR HEAT RATES TO EXTERNAL SURFACES AT 1 A.U., RTG-POWERED CONFIGURATION

Description	Node	Projected Area, A_p (in. ²)	α_s	Heat Rate Relation Used	Heat Rate (Btu/sec)	Comments
Dipole Antenna and Reflector	17	24	0.08	A-1	1.65×10^{-3}	OSR surfaces degraded from $\alpha_s = 0.04$ to 0.08 due to curvature of surface
	18	52	0.08		3.56×10^{-3}	
	19	52	0.08		3.56×10^{-3}	
OSR Arrays	20	152	0.25	A-1	3.25×10^{-2}	White paint on reflector section of antenna
	21	152	0.25		3.25×10^{-2}	
OSR Band	27	298	0.04	A-1	1.02×10^{-2}	
	40	522	0.04		1.79×10^{-2}	
Two Booms	34	208	0.04	A-1	7.12×10^{-3}	Two booms combined and divided into three radial lengths with OSR surfaces assumed degraded from $\alpha_s = 0.04$ to 0.08 because of surface curvature
	35	8.6	0.08	A-2	5.90×10^{-4}	
	36	17.2	0.08		1.18×10^{-3}	
RTG Booms	37	25.0	0.08		1.71×10^{-3}	The booms combined and divided into three radial lengths with OSR surfaces assumed degraded from $\alpha_s = 0.04$ to 0.08 because of surface curvature
	42	8.6	0.08	A-2	5.90×10^{-4}	
	43	17.2	0.08		1.18×10^{-3}	
Five Sun Sensors	44	80.0	0.08		5.48×10^{-3}	White paint plus holes
	28	20.75	0.4	A-2	2.26×10^{-3}	
Experiment No. 4 and No. 6	29	11.20	0.1	A-2	3.05×10^{-4}	OSR plus holes
Experiment No. 7	30	0.65	1.0	A-2	1.75×10^{-4}	Opening assumed to be blackbody
Experiment No. 2	31	14.10	0.5	A-2	1.92×10^{-3}	Aluminum plus holes

Table A-3
HEAT SOURCES INTERNAL TO VEHICLE

Equipment	Node	Power (W)	Heat Rate (Btu/sec)
DTU box located over gas bottle	3	1.0	9.48×10^{-4}
All other equipment on platform	4	46.0	4.37×10^{-2}
Experiment No. 2	5	0.5	4.74×10^{-4}
Experiment No. 7	6	1.0	9.48×10^{-4}
Experiments No. 4 and 6	7	2.6	2.47×10^{-3}
Two RTG Units ^(a)	44	1200	1.138

(a) Pertains to RTG-powered configuration only.

0.010-in. -thick fiberglass facing sheets, the following relation for conduction resistance was used:

$$R_{ij} \left(\frac{\text{sec-}^\circ \text{F}}{\text{Btu}} \right) = \frac{L}{W} (7.44 \times 10^5) \left(\frac{\text{sec-}^\circ \text{F}}{\text{Btu}} \right) \quad (\text{A. 4})$$

where L and W are as shown in Fig. A-2.

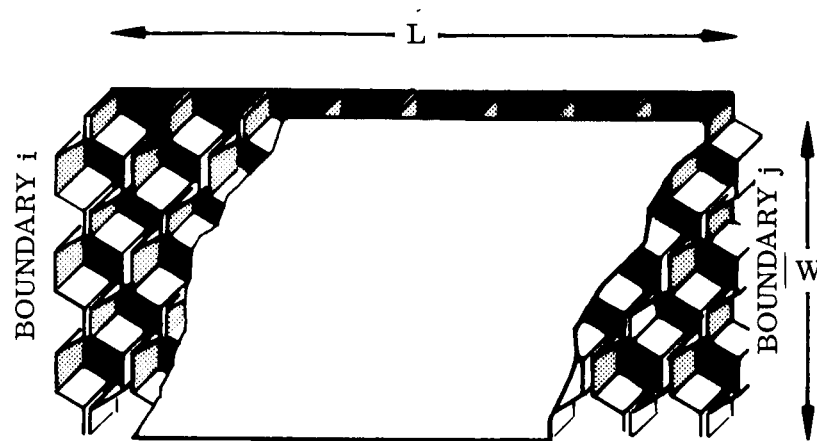


Fig. A-2 Honeycomb Schematic

Conduction resistances and specific assumptions used in their determination are given in Table A-4 for both the solar-powered and RTG-powered configurations. Resistances that are peculiar to each configuration are noted.

A.4 ENERGY EXCHANGE BY RADIATION

Radiant energy exchange between the various nodes was calculated by a finite-difference electrical analog method which uses a linearized radiation resistance defined by

$$R_{ij} \left(\frac{\text{sec-}^\circ \text{R}}{\text{Btu}} \right) = \frac{1}{(\text{RADK}_{ij}) \sigma (T_i^2 + T_j^2) (T_i + T_j)}$$

Table A-4

THERMAL CONDUCTION RESISTANCES

Resistor No.	Node Description	Connecting Nodes i-j	Resistance Value (°F sec/Btu)	Assumptions
1	Antenna Dipole	19-18	1.890×10^4	$L = 26$ in. { Al tubing, $L = 13$ in. { 2 in. O.D., 0.1 in. thick, $k = 100$ Btu/hr-ft-°F $L = 23$ in. { 55 Al tubes, $L = 11.5$ in. { 1/8 in. O.D., $A_x = 0.018$ in. ² /tube, $k = 100$
2	Antenna Dipole to Motor	18-16	9.45×10^3	
3	Antenna Reflector	21-20	1.000×10^4	
4	Antenna Reflector to Antenna Platform	20-17	5.10×10^3	
5	Antenna Platform Bearing	17-16	1.000×10^5	Estimated resistance across bearing and drive.
33 ^(a)	Antenna Motor to	16-15	3.33×10^3	{ Al tubing, $L = 7$ in., 3/4 in. O.D., $A_x = 0.3326$ in. ² /tube, $k = 100$. Contact resistance assumed to be 9×10^3 . Total resistance of one support = $R_1 = 1.0 \times 10^4$ Three supports are combined into one resistance by dividing R_1 by 3.
34 ^(a)	Boom Brackets	15-9	3.33×10^3	
37 ^(a)	Boom to Boom Brackets	35-9	3.33×10^2	
36 ^(a)	Boom	36-35	8.75×10^3	
35 ^(a)	Boom	37-36	8.75×10^3	{ Al tubing, $L = 30$ in., 1 in. O.D., $A_x = 0.494$ in. ² /tube, $k = 100$. Three booms combined.
38 ^(a)	Boom Brackets to Instrument Platform	9-10	3.46×10^4	Contact resistance assumed.
31	Outside to Exp. No. 2	31-5	1.0×10^2	Resistance actually < 100° F sec/Btu.
29	Outside to Exp. No. 7	30-6	<div>↓</div>	<div>↓</div>
27	Outside to Exps. No. 4 & 6	29-7		
25	Outside to Sun Sensor	28-8		
40	DTU Package to Platform	3-10		
39	All Other Equipment	4-10		
32	Experiment No. 2	5-10		
30	Experiment No. 7	6-10		
28	Experiments No. 4 and 6	7-10		
26	Sun Sensor Bracket	10-8		
41	Through Instrument Platform	10-11		
42	Platform to Cylinder	11-13	1.000×10^3	Magnesium, $L = 4.5$ in., $A_x = 0.785$ in. ² , $k = 70$.
43	Cylinder to Gas Bottle	13-2	8.30×10^5	Teflon, $L = 1.5$ in., $A_x = 0.785$ in. ² , $k = 0.1$.
24	Sun Sensor Bracket to Upper Solar Array	27-8	5.00×10^4	High resistance required to isolate array at 0.2 A.U. orbit.
Insulation Resistance Perpendicular to Layers:				
8	Top Cover	23-22	4.32×10^4	$L = 1/2$ in., $A_x = \pi(320)$ in. ² , multilayer $k = 5 \times 10^{-4}$
14	Top Array	25-26	3.58×10^4	$L = 3/8$ in., $A_x = \pi(36 \times 8)$ in. ² , { Multilayer $L = 1/8$ in., $A_x = \pi(36 \times 8)$ in. ² { $k = 5 \times 10^{-4}$
15		26-27	1.19×10^4	
19	Bellyband	32-33	2.11×10^4	$L = 3/8$ in., $A_x = \pi(36 \times 6.75)$ in. ² { Degraded $L = 1/8$ in., $A_x = \pi(36 \times 6.75)$ in. ² { multilayer $k = 10^{-3}$
20		33-34	7.1×10^3	
49	Bottom Array	38-39	2.04×10^4	$L = 3/8$ in., $A_x = \pi(36 \times 14)$ in. ² { Multilayer $L = 1/8$ in., $A_x = \pi(36 \times 14)$ in. ² { $k = 5 \times 10^{-4}$ $L = 3/8$ in., $A_x = \pi(36 \times 7.5)$ in. ² { $L = 1/8$ in., $A_x = \pi(36 \times 7.5)$ in. ² {
50		39-40	6.8×10^3	
54 ^(a)		41-42	3.82×10^4	
55 ^(a)		42-43	1.27×10^4	
44	Gas Bottle	2-14	8.50×10^4	$L = 1/4$ in., $A_x = 4\pi(4.5)^2$ in. ² Multilayer $k = 5 \times 10^{-4}$
45	Cylinder	12-13	1.70×10^5	$L = 1/2$ in., $A_x = \pi(10 \times 8)$ in. ² Multilayer $k = 5 \times 10^{-4}$

See footnotes at end of table, p. A-10.

Table A-4 (Cont.)

Resistor No.	Node Description	Connecting Nodes i-j	Resistance Value (*F sec/Btu)	Assumptions
Insulation Resistance Parallel to Layers:				
7	Top Cover	16-22	1.04×10^6	$L = 7 \text{ in.}$, $A_x = (1/2 \times \pi \times 18) \text{ in.}^2$, multilayer parallel to layers, $k = 0.01$.
6		16-23	1.04×10^6	
10		24-22	4.85×10^5	
9		24-23	4.85×10^5	
11	Upper Array Insulation	24-25	6.16×10^5	$L = 9 \text{ in.}$, $A_x = (1/2 \times \pi \times 36) \text{ in.}^2$, multilayer parallel to layers, $k = 0.01$.
12		24-26	6.16×10^5	
13	Upper Array Honeycomb Substrate	24-27	2.63×10^4	$R = L/W(7.44 \times 10^5)$, $L = 4 \text{ in.}$, $W = (\pi \times 36) \text{ in.}$
16	Upper Array to Bellyband	25-32	1.127×10^6	$L = 7.375 \text{ in.}$, $A_x = (1/4 \times \pi \times 36) \text{ in.}^2$, $k = 0.01$.
17		26-33	1.127×10^6	
18		27-34	6.0×10^6	
21	Bellyband Insulation to Instrument Platform	32-10	5.2×10^5	Assumed high resistance because no direct connection.
22		33-10	5.2×10^5	
23		34-10	6.0×10^6	
46	Instrument Platform to Lower Insulation	11-38	1.076×10^6	$L = 7 \text{ in.}$, $A_x = (1/4 \times \pi \times 36)$, $k = 0.01$.
47		11-39	1.076×10^6	
48	Lower Array Honeycomb Substrate	11-40	4.61×10^4	$R = L/W(7.44 \times 10^5)$, $L = 7 \text{ in.}$, $W = \pi(36) \text{ in.}$
51(a)	Lower Insulation	38-41	1.646×10^6	$L = 10.75 \text{ in.}$, $A_x = (1/4 \times \pi \times 36) \text{ in.}^2$, $k = 0.01$.
52(a)		39-42	1.646×10^6	
53(a)	Lower Array Honeycomb Substrate	40-43	7.08×10^4	$R = L/W(7.44 \times 10^5)$, $L = 10.75 \text{ in.}$, $W = \pi(36) \text{ in.}$
33(b)	Antenna Base & Motor to Boom Brackets	16-15	5.0×10^3	Al tubing, $L = 7 \text{ in.}$, $3/4 \text{ in. O.D.}$, $A_x = 0.3326 \text{ in.}^2/\text{tube}$, $k = 100$. Contact resistance assumed to be 9×10^3 . Total resistance of one support = $R_1 = 1.0 \times 10^4$. Two supports are combined into one resistance by dividing R_1 by 2.
34(b)		15-9	5.0×10^3	
55(b)		45-41	5.0×10^3	
56(b)		45-16	5.0×10^3	
37(b)	Boom Brackets to Experiment Booms	35-9	5.0×10^2	Contact resistance assumed.
36(b)		36-35	1.310×10^4	
35(b)		37-36	1.310×10^4	
53(b)	Boom Brackets to RTG Booms	42-41	5.0×10^2	Contact resistance assumed.
52(b)		43-42	1.310×10^4	
51(b)		44-43	1.310×10^4	
38(b)	Boom Brackets to Platform	9-10	5.20×10^4	Al tubing, $L = 30 \text{ in.}$, 1 in. O.D. , $A_x = 0.494 \text{ in.}^2$, $k = 100$. Two booms combined.
54(b)		41-10	5.20×10^4	

(a) Indicates resistance values peculiar to solar-powered configuration.

(b) Indicates resistance values peculiar to RTG-powered configuration.

where

$$\text{RADK}_{ij} \equiv \frac{A_i F_{a,ij} F_{e,ij}}{3600} \left(\frac{\text{ft}^2 \cdot \text{hr}}{\text{sec}} \right)$$

$$F_{e,ij} \doteq \epsilon_i \epsilon_j$$

All radiant exchange factors, RADK_{ij} , can be calculated in a straightforward manner using the above relations except the following:

- (1) Radiation between the louver system, with its variable effective emittance imaginary surface, and all surfaces which "see" the louver system
- (2) The lower solar cell array, which has only half of its surface area exposed to space

The louver system effective emittance is a linear function of lower platform temperature as plotted in Fig. A-3.

Radiation exchange factors, RADK_{ij} , and specific assumptions used in their determination are given in Table A-5 for both the solar-powered and RTG-powered configurations. Radiation exchange factors that are peculiar to each configuration are noted.

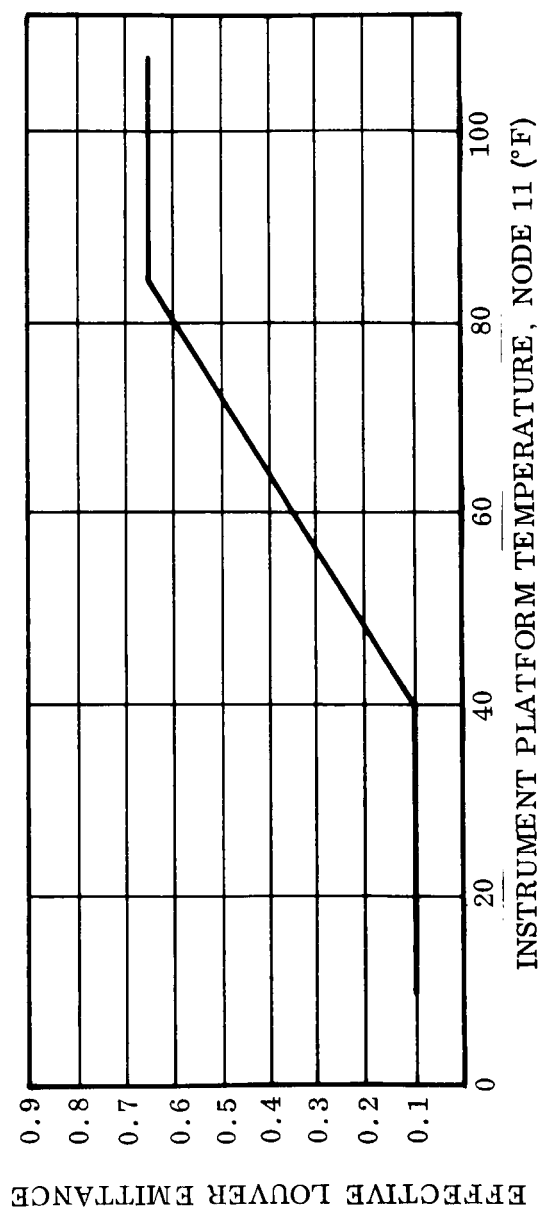


Fig. A-3 Effective Louver Emittance as a Function of Instrument Platform Temperature

Table A-5
THERMAL RADIATION EXCHANGE FACTORS

Resistor No.	Connecting Nodes		RADK _{ij} ($\frac{\text{ft}^2\text{-hr}}{\text{sec}}$)	Radiative Characteristics				Comments
	i	j		ϵ_i	ϵ_j	F_{ij}	A_i (in. ²)	
101	21 (Antenna Reflector)	1 (Space)	0.297×10^{-3}	0.85	1.0	0.84	215	White paint
102	21	1	0.315×10^{-3}	0.80		0.95	215	OSR
103	20	1	0.218×10^{-3}	0.85		0.62	215	White paint
104	20	1	0.249×10^{-3}	0.80		0.75	215	OSR
105	19 (Antenna Dipole)	1	1.460×10^{-4}	0.80		0.63	150	OSR
106	18	1	1.110×10^{-4}	0.80		0.48	150	OSR
107	17 (Antenna Platform)	1	0.954×10^{-4}	0.05		0.79	190	Polished Al
108	23 (Top Cover)	1	0.890×10^{-4}	0.05		0.84	1100	Al side of multilayer insul.
109	24 (Top Ring)	1	1.250×10^{-5}	0.05		1.00	130	Polished Al
110(a)	27 (Upper Solar Cell Array)	1	1.490×10^{-3}	0.82			940	Solar cells
119(a)	40 (Lower Solar Cell Array)	1	1.300×10^{-3}	0.82			825	Solar cells, 1/2 array shielded
124(a)	43	1	0.700×10^{-3}	0.82			442	Solar cells, 1/2 array shielded
115	34 (Bellyband)	1	1.150×10^{-3}	0.80			747	OSR
111	28 (Sun Sensors)	1	0.320×10^{-4}	0.80			20.75	White paint with holes
112	29 (Exps. No. 4 and 6)	1	1.730×10^{-5}	0.80			11.2	OSR with holes
113	30 (Exp. No. 7)	1	1.240×10^{-6}	1.00			0.646	Opening assumed to be blackbody
114	31 (Exp. No. 2)	1	0.273×10^{-5}	0.10			14.1	Al with holes
116(a)	35 (Booms)	1	0.988×10^{-4}	0.80		0.75	85.0	OSR - 1/4 of length
117(a)	36	1	0.262×10^{-3}	0.80		1.00	170.0	OSR - 1/2 of length
118(a)	37	1	1.310×10^{-4}	0.80		1.00	85.0	OSR - 1/4 of length
120	38 (Lower Array Insulation)	1	0.223×10^{-4}	0.05		0.206	1120	Al side of multilayer insul.
123(a)	41	1	0.219×10^{-4}	0.05		0.266	850	Al side of multilayer insul.
122	12 (Cylinder Outside)	1	1.830×10^{-6}	0.05		0.083	227	Al side of multilayer insul.
126	13 (Cylinder Inside)	1	0.525×10^{-5}	0.17		$F_{ij}A_i = 16.0$		Mg cylinder, bottom removed
127	14 (Sphere)	1	0.290×10^{-5}	0.05		$F_{ij}A_i = 30.0$		Al side of multilayer insul.
121	11 (Louvers)	1	1.32×10^{-4} to 9.90×10^{-4}	0.10 to 0.75		0.340	690	RADK _{ij} and ϵ_i are linear functions of node 11 temp. from 39°F (closed) to 85°F (open)
123(b)	42 (RTG)	1	0.650×10^{-4}	0.80		0.75	56	OSR
124(b)	43 (Booms)	1	1.740×10^{-4}			1.00	113	
125(b)	44 (Booms)	1	0.247×10^{-2}			1.00	1600	
116(b)	35 (Experiment)	1	0.650×10^{-4}			0.75	56	
117(b)	36 (Booms)	1	1.740×10^{-4}			1.00	113	
118(b)	37 (Booms)	1	0.862×10^{-4}				56	
110(b)	27 (Upper Array)	1	1.450×10^{-3}				940	
119(b)	40 (Lower Array)	1	0.255×10^{-2}				1650	OSR
201	18 (Dipole)	17 (Ant. Platform)	1.730×10^{-6}		0.05	0.15	150	
202		20 (Reflector)	0.354×10^{-4}		0.85	0.18	150	

See footnotes at end of table, p. A-15.

Table A-5 (Cont.)

Resistor No.	Connecting Nodes		RADK _{ij} ($\frac{\text{ft}^2\text{-hr}}{\text{sec}}$)	Radiative Characteristics				Comments
	i	j		ϵ_i	ϵ_j	F _{ij}	A _i (in. ²)	
203	18 (Dipole)	21 (Reflector)	0.786×10^{-5}	0.80	0.85	0.04	150	
204	↓	23 (Top Cover Outside)	1.730×10^{-6}	↓	0.05	0.15	↓	
205	19 (Dipole)	17 (Antenna Platform)	0.462×10^{-6}	↓	0.05	0.04	↓	
206	↓	20 (Reflector)	0.255×10^{-4}	↓	0.85	0.13	↓	
207	↓	21 (Reflector)	0.296×10^{-4}	↓	0.85	0.15	↓	
208	↓	23 (Top Cover Outside)	0.462×10^{-6}	↓	0.05	0.04	↓	
209	23 (Top Cover Outside)	20 (Reflector)	0.395×10^{-5}	0.05	0.85	0.10	482	Front of reflector
210	↓	20 (Reflector)	0.432×10^{-5}	↓	0.80	0.14	400	Back of reflector
211	↓	21 (Reflector)	0.395×10^{-6}	↓	0.85	0.01	482	Front of reflector
212	↓	21 (Reflector)	0.922×10^{-6}	↓	0.80	0.03	400	Back of reflector
213	17 (Platform)	20 (Reflector)	0.205×10^{-5}	↓	0.85	0.13	192	Front of reflector
214	↓	21 (Reflector)	0.31×10^{-6}	↓	0.85	0.02	192	Front of reflector
215	↓	23 (Top Cover Outside)	0.925×10^{-6}	↓	0.05	1.00	192	
216	16 (Motor & Base)	25 (Upper Array Insulation)	0.310×10^{-6}	0.10	0.05	0.17	19	Base is 5-in. dia.
217	↓	32 (Bellyband Insulation)	1.460×10^{-7}	↓	0.05	0.08	↓	
218	↓	3 (DTU)	0.920×10^{-7}	↓	0.10	0.25	↓	A ₃ = 60 in. ²
219	↓	4 (Other Equipment)	0.550×10^{-7}	↓	0.10	0.15	↓	A ₄ = A ₁₀ = $\frac{\pi(18^2 - 5^2)}{2} - 80$ in. ²
220	↓	5 (Exp. No. 2)	0.180×10^{-7}	↓		0.05	↓	A ₅ = 24 in. ²
221	↓	6 (Exp. No. 7)	0.180×10^{-7}	↓		0.05	↓	A ₆ = 36 in. ²
222	↓	7 (Exps. No. 4 and 6)	0.370×10^{-7}	↓		0.10	↓	A ₇ = 80 in. ²
223	↓	10 (Exp. Platform)	0.550×10^{-7}	↓		0.15	↓	A ₄ = A ₁₀ = 430 in. ²
224	22 (Top Cover Inside)	25 (Upper Array Insulation)	1.540×10^{-6}	0.05	0.05	0.32	905	
225	22 (Top Cover Inside)	32 (Bellyband Insulation)	0.385×10^{-6}	↓	0.05	0.08	↓	
226	↓	3 (DTU)	0.964×10^{-6}	↓	0.10	0.10	↓	
227	↓	4 (Other Equipment)	1.450×10^{-6}	↓		0.15	↓	
228	↓	5 (Exp. No. 2)	0.482×10^{-6}	↓		0.05	↓	
229	↓	6 (Exp. No. 7)	0.482×10^{-6}	↓		0.05	↓	
230	↓	7 (Exps. No. 4 & 6)	0.964×10^{-6}	↓		0.10	↓	
231	↓	10 (Exp. Platform)	1.450×10^{-6}	↓		0.15	↓	
232	25 (Upper Array Insulation)	10 (Exp. Platform)	0.338×10^{-5}	↓		0.30	1060	
233	32 (Bellyband Insulation)	10 (Exp. Platform)	0.315×10^{-5}	↓	↓	0.40	740	
234	3 (DTU)	14 (Sphere)	0.290×10^{-6}	0.10	0.05	0.50	60	
235	14 (Sphere)	13 (Cylinder)	0.275×10^{-6}	0.05	0.17	0.70	240	
238	12 (Cylinder Outside)	38 (Lower Array Insulation)	0.438×10^{-5}	0.05	0.05	0.40	227	

See footnotes at end of table, p. A-15.

Table A-5 (Cont.)

Resistor No.	Connecting Nodes		RADK _{ij} ($\frac{\text{ft}^2\text{-hr}}{\text{sec}}$)	Radiative Characteristics				Comments
	i	j		ϵ_i	ϵ_j	F_{ij}	A_i (in. ²)	
240 ^(a)	12 (Cylinder Outside)	41 (Lower Array Insulation)	0.203×10^{-6}	0.05	0.05	0.17	247	RADK _{ij} and ϵ_i are linear functions of node 11 temp. from 39°F (closed) to 85°F (open)
236	11 (Louvers)	12 (Cyl. Outside)	0.666×10^{-6} to 0.500×10^{-5}	0.10 to 0.75		0.10	690	
237	11 (Louvers)	38 (Lower Array Insulation)	0.267×10^{-5} to 0.200×10^{-4}			0.40		
239 ^(a)	11 (Louvers)	41 (Lower Array Insulation)	1.000×10^{-6} to 0.750×10^{-5}			0.15		
239 ^(b)	44 (RTG's)	21 (Reflector)	0.950×10^{-5}	0.80	0.80	$F_{ij}A_i = 7.7$		
240 ^(b)		20 (Reflector)	0.950×10^{-5}			$F_{ij}A_i = 7.7$		F _{ij} A _i products were obtained by summing data of NASA Hr 4 BD of 2-4-66
241 ^(b)		19 (Dipole)	1.600×10^{-6}			$F_{ij}A_i = 1.3$		
242 ^(b)		18 (Dipole)	1.600×10^{-6}			$F_{ij}A_i = 1.3$		
243 ^(b)		27 (Upper Array)	0.430×10^{-5}			$F_{ij}A_i = 3.5$		
244 ^(b)		34 (Bellyband)	0.518×10^{-5}			$F_{ij}A_i = 4.2$		
245 ^(b)		40 (Lower Array)	0.950×10^{-5}			$F_{ij}A_i = 7.7$		

(a) Indicates RADK_{ij} values peculiar to solar-powered configuration.(b) Indicates RADK_{ij} values peculiar to RTG-powered configuration.

Appendix B
SPECULAR REFLECTION FROM RTG DISKS

The effect of specular reflection of solar energy from the RTG disks to the satellite bellyband section is determined from the ratio of energy reflected to the satellite bellyband section to energy directly impinging on the bellyband section for each revolution of the satellite. The method used is as follows:

- (1) Determine the limits for all possible reflections based on a disk of radius R_2 by a square of edge $2R_2$.
- (2) Determine the amount of energy reflected from a disk between the previously determined limits of satellite rotation.
- (3) Assume, as a conservative estimate, that all the energy reflected from the two disks impinges on the satellite. (Actually, some of this energy will be reflected to space.)
- (4) Determine the direct energy impinging on the satellite bellyband and divide into the estimate from (3), above.

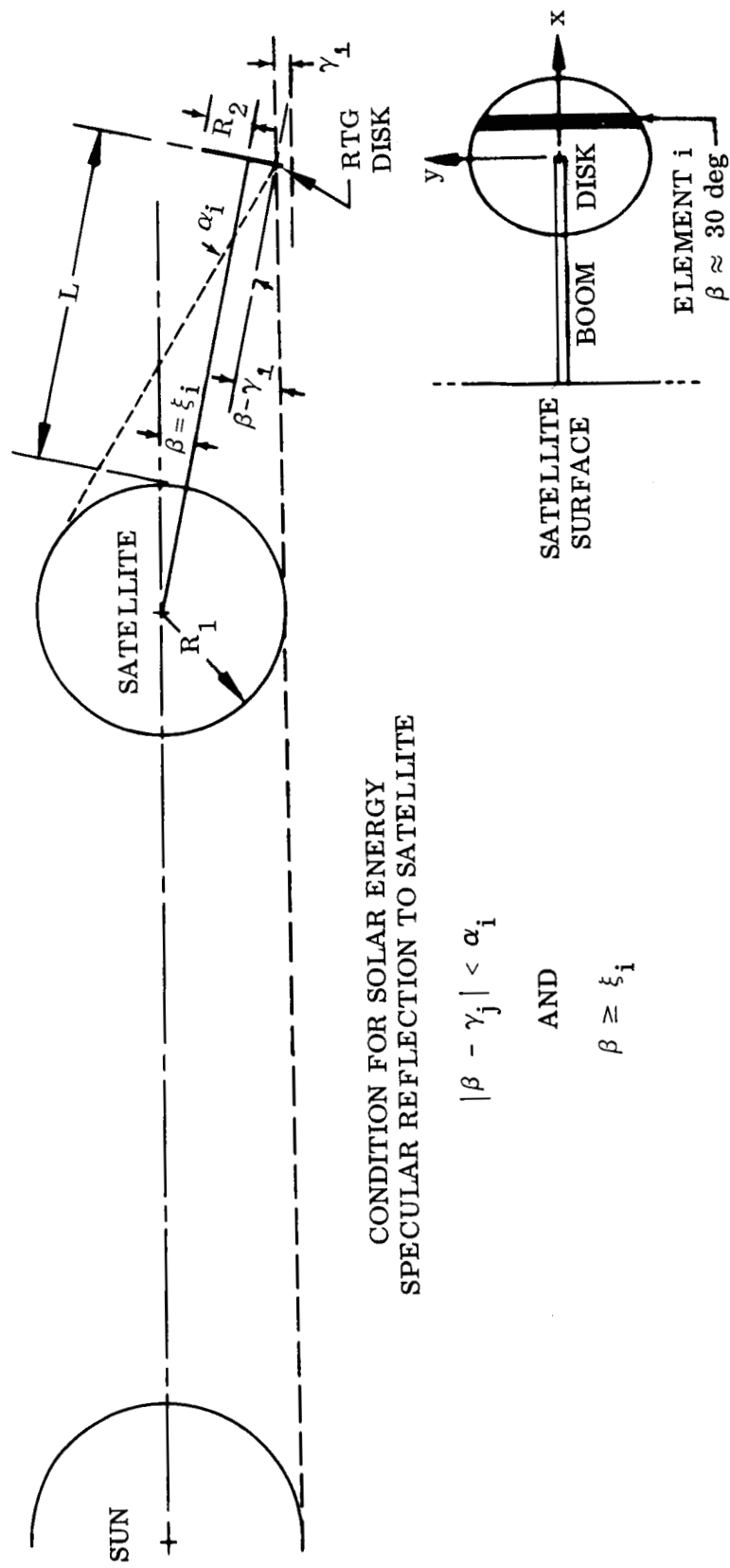
The dimensions used for the parameters described in Fig. B-1 are:

$$R_1 = 1.5 \text{ ft}$$

$$R_2 = 5 \text{ in.}$$

$$L = 5.0 \text{ ft}$$

$$\gamma_1 = 1.5 \text{ deg}$$



B-2

Fig. B-1 Specular Reflection Diagram

The condition for possible solar energy specular reflection to the satellite is:

Mathematical Condition

$$|\beta - \gamma_j| < \alpha_i$$

$$\beta > \xi_i$$

Physical Condition

Solar ray j angle of incidence to disk element i is less than the angle of reflection that will miss the satellite.

Disk element is illuminated by sun.

The limiting case is for $\beta = \xi_i$.

Determination of α_i for leading edge, center, and trailing edge of disk
(Approximate solution for leading and trailing edge)

$$\tan \alpha = \left(\frac{R_1}{\cos \alpha} + R_2 \right) / (R_1 + L)$$

<u>Point</u>	<u>R_2 (in.)</u>	<u>α (deg)</u>
Leading edge	+5	17.8
Center	0	13.35
Trailing edge	-5	9.6

Determination of $\xi_i - \gamma_j$ for leading edge, center, and trailing edge of disk
(Approximate solution)

Assuming the sun's rays to be parallel to the sun-satellite line:

$$\xi = \sin^{-1} \frac{R_1 - R_2 \cos \xi}{R_1 + L}$$

An approximation for ξ with $\gamma_j \neq 0$ and $\xi < 20$ deg is

$$\xi \doteq \sin^{-1} \left(\frac{R_1 + R_2 \cos \xi}{R_1 + L} \right) + \gamma_j$$

For $\gamma_j = 1.5$:

<u>Leading Edge</u>	<u>Center</u>	<u>Trailing Edge</u>
$\xi_i = 8.40$	11.85	16.5
$\xi_i - \gamma_j = 9.9$	13.35	18.0

Testing the limiting condition for reflected solar energy incident on the satellite,

$$\gamma_j < \alpha_i$$

Leading edge: 9.9 deg < 17.8 deg

Center: 13.35 deg = 13.35 deg

Trailing edge: 18.0 deg \nless 9.6 deg

The period of possible reflections incident on spacecraft is

$$8.4 \text{ deg} < \beta < 11.85 \text{ deg}$$

$$0 < t < 0.0096 \text{ sec}$$

where $t = 0$ is defined when $\beta = 8.4 \text{ deg}$.

To compute the total energy reflected from the disk, the instantaneous disk area illuminated was determined as a function of time and then integrated over the limiting reflection period. The result is an integrated time-area which is multiplied by $\cos \beta_{\text{ave}}$ to obtain the time-projected area. The maximum total energy reflected from the disk per satellite revolution is given by

$$Q_T = K\rho(\text{time-projected area}) G_s 0.2 \text{ A. U.}$$

where

$$K = \text{number of reflection occurrences per revolution} = 4$$

$$\rho = \text{disk reflectance} = 0.95$$

$$\text{time projected area} = \cos \beta_{\text{ave}} \int_0^t A(t) dt = 4.28 \times 10^{-7} \text{ ft}^2\text{-hr}$$

$$G_{s \text{ 0.2 A.U.}} = (25) \left(443 \frac{\text{Btu}}{\text{hr-ft}^2} \right) = 1.11 \times 10^4 \frac{\text{Btu}}{\text{hr-ft}^2}$$

The direct solar energy impinging on the satellite bellyband section is given by

$$Q = A_p G_{s \text{ 0.2 A.U.}}$$

where

$$A_p = \text{projected area of bellyband} = 1.5 \text{ ft}^2$$

$$T = \text{period revolution} = 1 \text{ sec}$$

$$\frac{QT}{QD} = K\rho \frac{(\text{time-projected area})}{A_p T}$$

$$= \frac{(4)(0.95)(4.28 \times 10^{-7})}{1.5 \frac{1}{3600}}$$

$$= 0.4 \text{ percent}$$

$$= \frac{QT}{T}$$

$$= 18 \times 10^{-3} \frac{\text{Btu}}{\text{sec}} = 19 \text{ W}$$

Definitions of Specular Reflection Terms

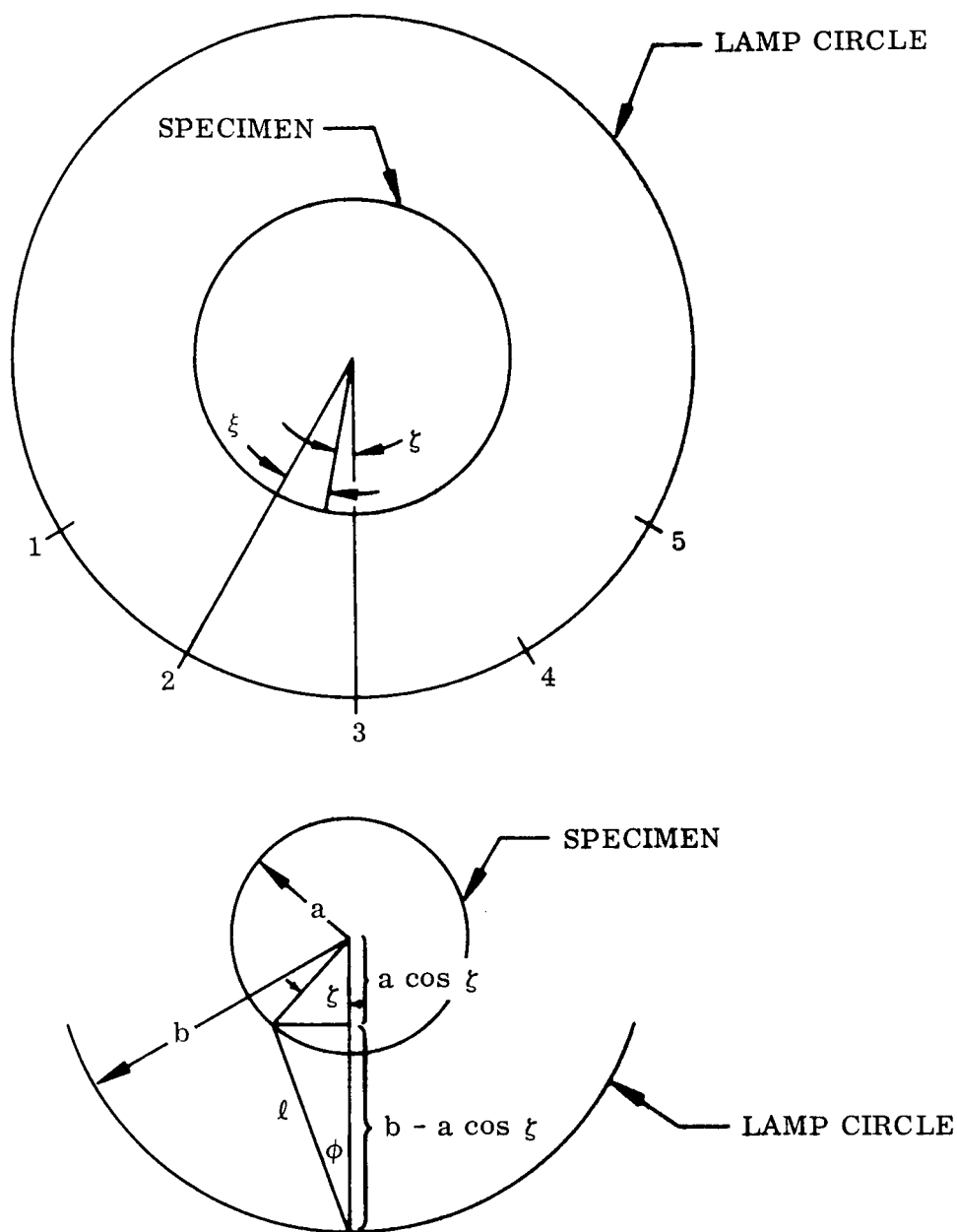
R_1	radius of cylindrical vehicle
R_2	radius of OSR disk; positive at leading edge, negative at trailing edge
L	distance from surface of vehicle to OSR-coated disk
α_i	angle between tangent to surface of cylindrical vehicle through an element i of the OSR coated disk and normal to the disk
β	angle to the centerline of the RTG boom, measured positive clockwise from sun-satellite line
ξ_i	β angle at which an element i of the OSR-coated disk just enters sunlight
γ_j	angle to a sun's ray j , measured positive clockwise from sun-satellite line
ρ	RTG disk reflectance
A	disk area
x, y	coordinate axes of disk
A_p	bellyband projected area
T	period of satellite revolution
t	time

Appendix C

INCIDENT HEAT FLUX VARIATION ON A CYLINDRICAL SURFACE EXPOSED
TO REFLECTED AND NONREFLECTED LINE SOURCES

The geometric arrangement of the energy sources and the test specimen will, in general, determine the overall uniformity of energy flux incident on the test specimen. To examine the effect of lamp-to-specimen distance and lamp spacing on incident flux uniformity, a brief analysis of the energy distribution resulting from line energy sources was performed for lamps with and without reflectors. Depending on the ratio of lamp circle diameter to specimen diameter and the location of a differential area on the cylindrical specimen, a differential area may view one or more lamps. This is illustrated in Fig. C-1.

The energy distribution on a cylindrical surface resulting from a line source is calculated in Tables C-1 through C-3 and is plotted in Figs. C-2, C-3, and C-4 as a function of the angle ζ about the cylinder axis. This is done for two assumed angular intensity distributions and one case of uniform intensity variation about the source axis. The case of constant angular intensity variation corresponds to that from a lamp without a reflector or one with a very accurately located reflector. The case where the angular dependence is of the form $\exp(\phi/\phi_0) \cos \phi$ results in an energy distribution on the cylinder similar to what has been observed in practice. The analysis was performed for assumed cylinder radii of 15 and 30 in. and a lamp circle radius of 54 in. From the results shown in Figs. C-2, C-3, and C-4, the individual effects of each lamp in the array may be summed to yield the total intensity distribution as a function of position on the cylindrical surface. This is done in Tables C-4, C-5, and C-6. These results show that for all cases except the $\exp(\phi/\phi_0) \cos \phi$ variation on the 30-in. cylinder the energy variation in the circumferential direction is essentially uniform. Also, for the range of cylinder radii examined, the heat flux variation for the cosine source variation and the uniform source case is substantially independent of cylinder radius. The flux variation with radius for the $\exp(\phi/\phi_0) \cos \phi$ case is from 8 to 31 percent.



$$\phi = \tan^{-1} \frac{a \sin \xi}{b - a \cos \xi}$$

$$\begin{aligned} \ell &= [(a \sin \xi)^2 + (b - a \cos \xi)^2]^{1/2} \\ &= [a^2 \sin^2 \xi + b^2 - 2ab \cos \xi + a^2 \cos^2 \xi]^{1/2} \\ &= [a^2 + b^2 - 2ab \cos \xi]^{1/2} \end{aligned}$$

Fig. C-1 Lamp Array Geometry

Table C-1

ENERGY DISTRIBUTION ON A CYLINDRICAL SURFACE FOR A COSINE
VARIATION IN INTENSITY ABOUT THE AXIS OF LINE SOURCE

a	ξ	$b \cos \xi$	$a \cos \xi$	$b - a \cos \xi$	$b \cos \xi - a$	$a^2 + b^2 - 2ab \cos \xi$	$f(a, b, \xi)$	$\frac{f(a, b, \xi)}{f(30, b, 0)}$
30	0	54	30	24	24	580	0.0412	1
	10	53.2	29.6	24.4	23.2	630	0.0358	0.870
	20	50.7	28.2	25.8	20.7	770	0.0251	0.610
	30	46.8	26.0	28.0	16.8	1010	0.0147	0.357
	40	41.3	23.0	31.0	11.3	1340	0.00713	0.173
	50	34.7	19.3	34.7	4.7	1740	0.00196	0.0477
15	0	54	15.0	39	39	1525	0.0253	0.615
	10	53.2	14.8	39.2	38.2	1550	0.0246	0.598
	20	50.7	14.1	39.9	35.7	1623	0.0219	0.532
	30	46.8	13.0	41.0	31.8	1742	0.0179	0.435
	40	41.3	11.5	42.5	26.3	1905	0.01295	0.315
	50	34.7	9.65	44.3	19.7	2105	0.00847	0.206
	60	27.0	7.50	46.5	12.0	2335	0.00494	0.120
	70	18.5	5.13	48.9	3.5	2590	0.0013	0.0316

Table C-2

ENERGY DISTRIBUTION ON A CYLINDRICAL SURFACE AS RECEIVED
FROM LINE SOURCE RADIATING UNIFORMLY IN ALL DIRECTIONS

a	ζ	$b \cos \zeta - a$	$a^2 + b^2 - 2ab \cos \zeta$	$g'(a, b, \zeta) = \frac{1}{2}$	$\frac{g'(a, b, \zeta)}{g'(30, b, \zeta)}$
30	0	24	580	0.0413	1
	10	23.2	630	0.0368	0.892
	20	20.7	770	0.0269	0.65
	30	16.8	1010	0.01665	0.403
	40	11.3	1340	0.00844	0.204
	50	4.7	1740	0.0027	0.0653
15	0	39	1525	0.0257	0.622
	10	38.2	1550	0.0246	0.595
	20	35.7	1623	0.0220	0.533
	30	31.8	1742	0.01825	0.442
	40	26.3	1905	0.0138	0.334
	50	19.7	2105	0.00937	0.227
	60	12.0	2335	0.00513	0.124
	70	3.5	2590	0.00135	0.0327

Table C-3

ENERGY DISTRIBUTION ON A CYLINDRICAL SURFACE FOR AN INTENSITY
 VARIATION OF $e^{-(6\phi/\pi)} \cos \phi$ ABOUT THE AXIS OF A LINE SOURCE

a	ζ	f(a, b, ζ)	$e^{-(6\phi/\pi)}$	$\frac{g(a, b, \zeta)}{g(30, b, 0)}$
30	0	0.0412	1	1
	10	0.0358	0.653	0.568
	20	0.0251	0.483	0.300
	30	0.0147	0.40	0.142
	40	0.00713	0.338	0.0588
	50	0.00196	0.327	0.0156
15	0	0.0253	1	0.625
	5		0.938	0.576
	10	0.0246	0.880	0.525
	20	0.0219	0.783	0.413
	30	0.0179	0.708	0.310
	40	0.01295	0.653	0.214
	50	0.00847	0.617	0.135
	60	0.00494	0.594	0.0713
	70	0.0013	0.586	0.0182

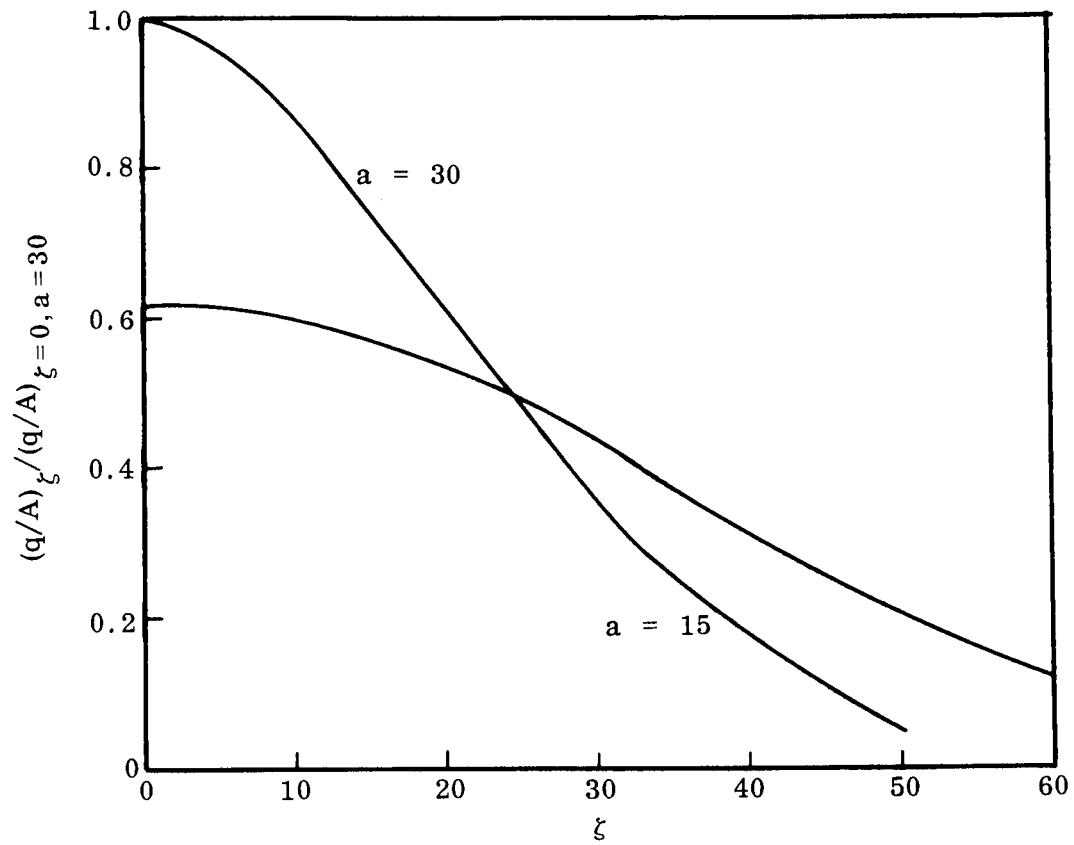


Fig. C-2 Energy Distribution on Cylindrical Surface.
Source intensity varies about source axis
as $\cos \phi$

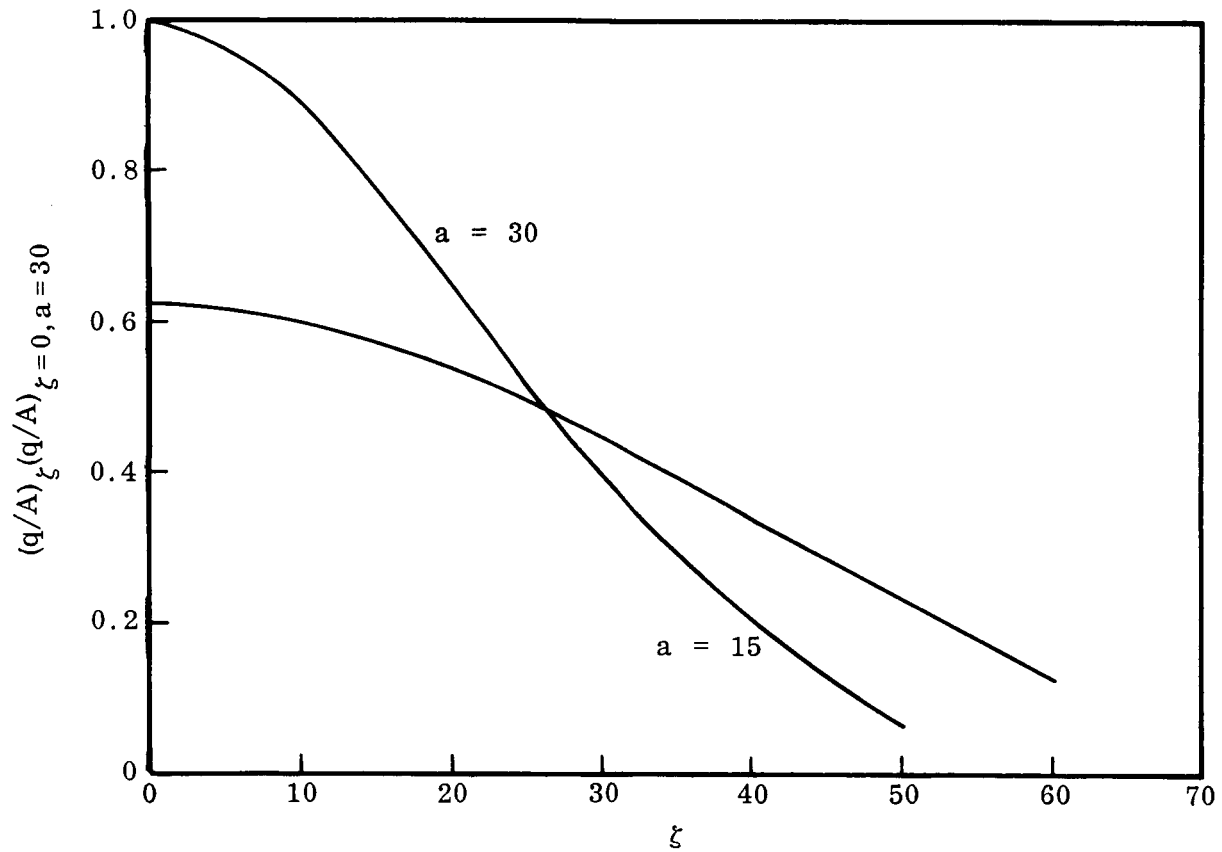


Fig. C-3 Energy Distribution on Cylindrical Surface. Source intensity uniform about source axis

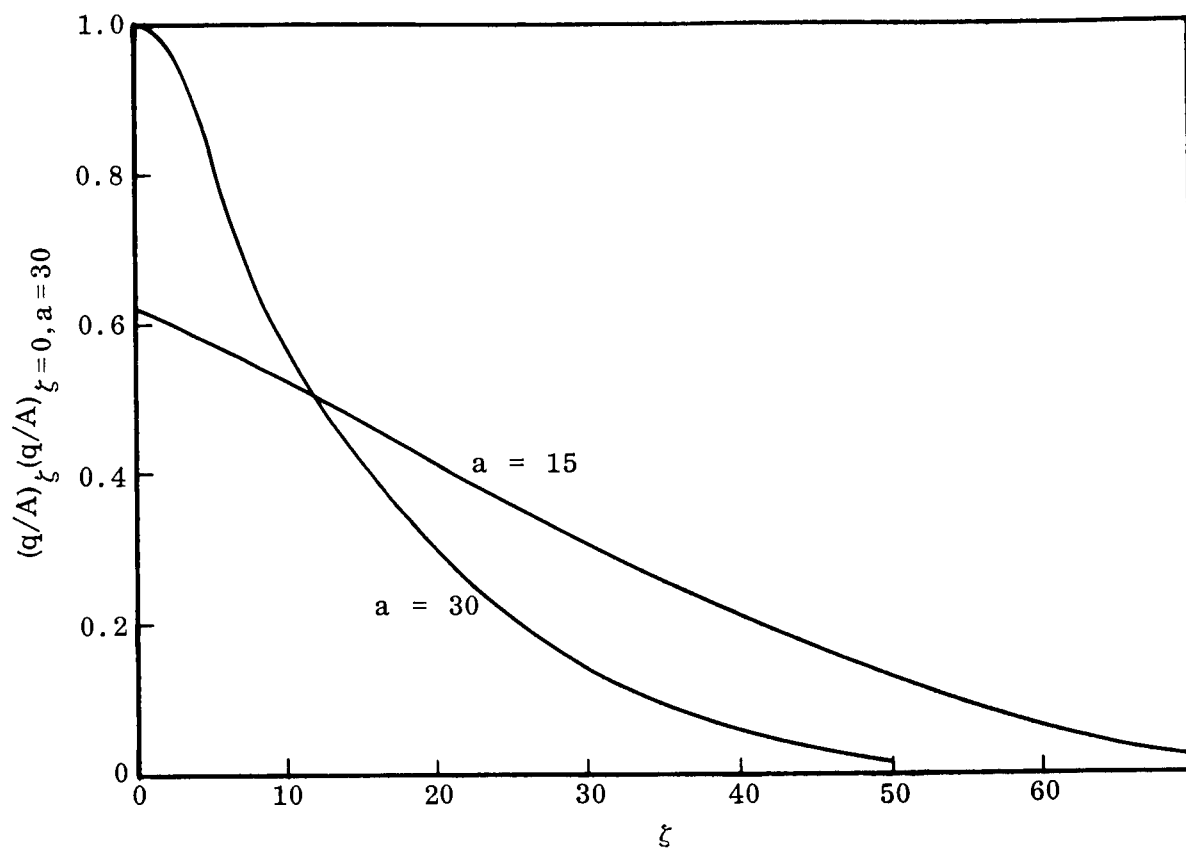


Fig. C-4 Energy Distribution on Cylindrical Surface. Source intensity varies about source axis according to $\exp - (6\phi/\pi) \cos \phi$

Table C-4

LAMP ANGLE AND HEAT FLUX FOR SPECIFIC LOCATIONS ON
SPECIMEN - COSINE INTENSITY VARIATION ABOUT SOURCE AXIS

a (in.)	Lamp No.	Lamp Angle, ξ				Heat Flux			
		Position on Specimen				Position			
		$\xi=0$	5	10	15	0	5	10	15
30	1	60	55	50	45	0	0	0.05	0.11
	2	30	25	20	15	0.35	0.46	0.60	0.76
	3	0	5	10	15	1.0	0.95	0.87	0.76
	4	30	35	40	45	0.35	0.255	0.18	0.11
	5	60	65	70	75	0	0	0	0
	Total					1.70	1.67	1.70	1.74
15	1	60	55	50	45	0.12	0.16	0.21	0.26
	2	30	25	20	15	0.435	0.49	0.53	0.57
	3	0	5	10	15	0.615	0.61	0.60	0.57
	4	30	35	40	45	0.435	0.375	0.315	0.26
	5	60	65	70	75	0.12	0.09	0.06	0.04
	Total					1.725	1.725	1.715	1.70

Table C-5
LAMP ANGLE AND HEAT FLUX FOR SPECIFIC LOCATIONS ON
SPECIMEN - INTENSITY UNIFORM ABOUT LAMP AXIS

a (in.)	Lamp No.	Lamp Angle, ξ				Heat Flux			
		Position on Specimen				Position			
		$\xi = 0$	5	10	15	$\xi = 0$	5	10	15
30	1	60	55	50	45	0	0.03	0.07	0.13
	2	30	25	20	15	0.40	0.52	0.65	0.775
	3	0	5	10	15	1.0	0.98	0.89	0.775
	4	30	35	40	45	0.40	0.30	0.205	0.13
	5	60	65	70	75	0	0	0	0
		Total				1.80	1.83	1.815	1.81
15	1	60	55	50	45	0.125	0.175	0.23	0.28
	2	30	25	20	15	0.445	0.49	0.535	0.57
	3	0	5	10	15	0.620	0.615	0.595	0.57
	4	30	35	40	45	0.445	0.39	0.335	0.28
	5	60	65	70	75	0.125	0.08	0.04	0
		Total				1.76	1.75	1.735	1.70

Table C-6

LAMP ANGLE AND HEAT FLUX FOR SPECIFIC LOCATIONS ON
SPECIMEN - $e^{-(6\phi/\pi)} \cos \phi$ INTENSITY VARIATION ABOUT SOURCE AXIS

a (in.)	Lamp No.	Lamp Angle, ξ				Heat Flux			
		Position on Specimen				Position			
		$\xi=0$	5	10	15	$\xi=0$	5	10	15
30	1	60	55	50	45	0	0.01	0.015	0.030
	2	30	25	20	15	0.14	0.215	0.3	0.415
	3	0	5	10	15	1.0	0.805	0.57	0.415
	4	30	35	40	45	0.14	0.090	0.06	0.030
	5	60	65	70	75	0	0	0	0
				Total		1.28	1.12	0.95	0.89
15	1	60	55	50	45	0.07	0.105	0.14	0.175
	2	30	25	20	15	0.31	0.36	0.42	0.47
	3	0	5	10	15	0.625	0.575	0.52	0.47
	4	30	35	40	45	0.31	0.26	0.215	0.175
	5	60	65	70	75	0.07	0.04	0.015	0
				Total		1.385	1.340	1.310	1.290

C.1 CASE I: ENERGY DISTRIBUTION AS A FUNCTION OF ANGLE FOR A COSINE SOURCE

C.1.1 Source Distribution

We assume that the relative intensity varies as $\cos \phi$:



$$\frac{E}{E_o} = \cos \phi$$

The total energy between any two values of ϕ is

$$\begin{aligned} E_T \frac{\int_{\phi_1}^{\phi_2} \frac{E}{E_o} d\phi}{\int_{-\pi/2}^{+\pi/2} \frac{E}{E_o} d\phi} &= E_T \frac{\int_{\phi_1}^{\phi_2} \cos \phi d\phi}{\int_{-\pi/2}^{+\pi/2} \cos \phi d\phi} \\ &= \frac{E_T}{2} (\sin \phi_2 - \sin \phi_1) \end{aligned}$$

$$\sin \phi_2 - \sin \phi_1 = 2 \cos \frac{1}{2} (\phi_2 + \phi_1) \sin \frac{1}{2} (\phi_2 - \phi_1)$$

If ϕ is small,

$$\sin \Delta\phi/2 \approx \Delta\phi/2$$

$$\sin \phi_2 - \sin \phi_1 \approx \frac{z\Delta\phi}{z} \cos \phi$$

$$\frac{\Delta E}{\Delta\phi} = \frac{1}{2} E_T \cos \phi$$

where

$$\Delta E/\Delta\phi = \text{power/degree at angle } \phi$$

$$E_T = \text{total source power}$$

C. 1. 2 Surface Distribution

$$\frac{dq}{dA} = \left(\frac{dE}{d\phi} \right) \left(\frac{d\phi}{d\xi} \right) \left(\frac{d\xi}{dA} \right)$$

$$\frac{dE}{d\phi} = \left(\frac{1}{2} \right) E_T \cos \phi = \frac{E_T}{2} \frac{b - a \cos \xi}{[a^2 + b^2 - 2ab \cos \xi]^{1/2}}$$

$$\frac{d\phi}{d\xi} = \frac{ab \cos \xi - a^2}{a^2 + b^2 - 2ab \cos \xi}$$

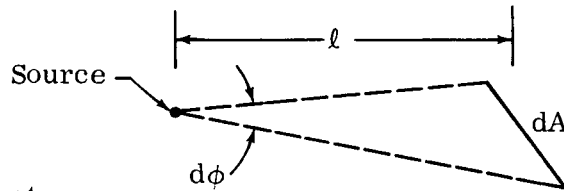
$$\frac{d\xi}{dA} = \frac{12}{a}$$

$$\begin{aligned} \frac{dq}{dA} &= \frac{(6)(E_T)(b \cos \xi - a)(b - a \cos \xi)}{[a^2 + b^2 - 2ab \cos \xi]^{3/2}} \\ &= (6)(E_T) f(a, b, \xi) \end{aligned}$$

C. 2 CASE II: UNIFORM IRRADIATION

C. 2. 1 Source Distribution

$$\frac{dE}{d\phi} = \text{const.}$$



C. 2. 2 Surface Distribution

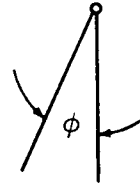
$$\frac{dq}{dA} = \left(\frac{dE}{d\phi} \right) \left(\frac{d\phi}{d\xi} \right) \left(\frac{d\xi}{dA} \right)$$

$$\frac{(dq/dA)_{\xi}}{(dq/dA)_{\xi=0}} = \frac{(d\phi/d\xi)_{\xi}}{(d\phi/d\xi)_{\xi=0}} = \frac{\frac{ab \cos \xi - a^2}{a^2 + b^2 - 2ab \cos \xi}}{\frac{ab - a^2}{a^2 + b^2 - 2ab}}$$

C.3 CASE III: SOURCE HAVING DISTRIBUTION CHARACTERIZED BY $\cos \phi \exp (\phi / \phi_0)$

C.3.1 Source Distribution

We assume that the relative intensity varies as



$$\frac{E_{\phi}}{E_{\phi=0}} = e^{-(6\phi/\pi)} \cos \phi$$

The total energy between 0 and ϕ is

$$\begin{aligned} \frac{E_T \int_0^{\phi} e^{-(6\phi/\pi)} \cos \phi}{2 \int_0^{\pi/2} e^{-(6\phi/\pi)} \cos \phi} &= \frac{E_T \frac{e^{-(6\phi/\pi)}}{1 + (36/\pi)} \left(-\frac{6}{\pi} \cos \phi + \sin \phi \right) \Big|_0^{\phi}}{\frac{e^{-(6\phi/\pi)}}{1 + (36/\pi)} \left(-\frac{6}{\pi} \cos \phi + \sin \phi \right) \Big|_0^{\pi/2}} \\ &= \frac{E_T}{(2) \left(e^{-3} + \frac{6}{\pi} \right)} \left\{ e^{-(6\phi/\pi)} \left(-\frac{6}{\pi} \cos \phi + \sin \phi \right) - \left(-\frac{6}{\pi} \right) \right\} \end{aligned}$$

The differential with respect to ϕ is

$$\begin{aligned} \frac{dE}{d\phi} &= \frac{E_T}{2 \left(e^{-3} + \frac{6}{\pi} \right)} \left\{ -\frac{6}{\pi} e^{-(6\phi/\pi)} \left(-\frac{6}{\pi} \cos \phi + \sin \phi \right) \right. \\ &\quad \left. + e^{-(6\phi/\pi)} \left(\frac{6}{\pi} \sin \phi + \cos \phi \right) \right\} \\ &= \frac{E_T}{2 \left(e^{-3} + \frac{6}{\pi} \right)} e^{-(6\phi/\pi)} \left(1 + \frac{36}{\pi^2} \right) \cos \phi \end{aligned}$$

C.3.2 Surface Distribution

$$\frac{dq}{dA} = \frac{dE}{d\phi} \frac{d\phi}{d\xi} \frac{d\xi}{dA}$$

$$\frac{dE}{d\phi} = \frac{1 + \frac{36}{\pi^2} \frac{E_T}{e^{-3} + \frac{6}{\pi}} e^{-(6\phi/\pi)} \cos \phi$$

$$= \frac{1 + \frac{36}{\pi^2} \frac{E_T}{e^{-3} + \frac{6}{\pi}} \exp \left\{ -\frac{6}{\pi} \tan^{-1} \frac{a \sin \xi}{b - a \cos \xi} \right\} \left\{ \frac{b - a \cos \xi}{\sqrt{a^2 + b^2 - 2ab \cos \xi}} \right\}$$

$$\frac{(dq/dA)_{\xi}}{(dq/dA)_{\xi=0}} = \frac{\exp \left\{ -\frac{6}{\pi} \frac{a \sin \xi}{b - a \cos \xi} \right\} \left\{ \frac{b - a \cos \xi}{\sqrt{a^2 + b^2 - 2ab \cos \xi}} \right\} \left\{ \frac{ab \cos \xi - a^2}{a^2 + b^2 - 2ab \cos \xi} \right\}}{\left(\frac{a}{b - a} \right)}$$

$$= \frac{\exp \left\{ -\frac{6}{\pi} \frac{a \sin \xi}{b - a \cos \xi} \right\} \{b - a \cos \xi\} \{b \cos \xi - a\} \{b - a\}}{\{a^2 + b^2 - 2ab \cos \xi\}^{3/2}}$$

$$= \exp \left\{ -\frac{6}{\pi} \frac{a \sin \xi}{b - a \cos \xi} \right\} \{b - a\} f(a, b, \xi)$$